

MIRD Pamphlet No. 16: Techniques for Quantitative Radiopharmaceutical Biodistribution Data Acquisition and Analysis for Use in Human Radiation Dose Estimates

Jeffrey A. Siegel, Stephen R. Thomas, James B. Stubbs, Michael G. Stabin, Marguerite T. Hays, Kenneth F. Koral, James S. Robertson, Roger W. Howell, Barry W. Wessels, Darrell R. Fisher, David A. Weber and A. Bertrand Brill
Nuclear Physics Enterprises, Cherry Hill, New Jersey; University of Cincinnati, Division of Medical Physics, Cincinnati, Ohio; Radiation Dosimetry Systems of Oak Ridge, Inc., Knoxville, Tennessee; Oak Ridge Institute for Science and Education, Radiation Internal Dose Information Center, Oak Ridge, Tennessee; Veterans Affairs Medical Center 640/151, Palo Alto, California; Department of Nuclear Medicine, University of Michigan, Ann Arbor, Michigan; Gaithersburg, Maryland; Division of Radiation Research, Department of Radiology, University of Medicine and Dentistry of New Jersey, Newark, New Jersey; Department of Radiology, George Washington University Medical Center, Washington, DC; Pacific Northwest National Laboratory, Richland, Washington; Department of Radiation Research, University of California Davis Medical Center, Sacramento, California; Department of Radiology, Vanderbilt University School of Medicine, Nashville, Tennessee

This report describes recommended techniques for radiopharmaceutical biodistribution data acquisition and analysis in human subjects to estimate radiation absorbed dose using the Medical Internal Radiation Dose (MIRD) schema. The document has been prepared in a format to address two audiences: individuals with a primary interest in designing clinical trials who are not experts in dosimetry and individuals with extensive experience with dosimetry-based protocols and calculational methodology. For the first group, the general concepts involved in biodistribution data acquisition are presented, with guidance provided for the number of measurements (data points) required. For those with expertise in dosimetry, highlighted sections, examples and appendices have been included to provide calculational details, as well as references, for the techniques involved. This document is intended also to serve as a guide for the investigator in choosing the appropriate methodologies when acquiring and preparing product data for review by national regulatory agencies. The emphasis is on planar imaging techniques commonly available in most nuclear medicine departments and laboratories.

The measurement of the biodistribution of radiopharmaceuticals is an important aspect in calculating absorbed dose from internally deposited radionuclides. Three phases are presented: data collection, data analysis and data processing. In the first phase, data collection, the identification of source regions, the determination of their appropriate temporal sampling and the acquisition of data are discussed. In the second phase, quantitative measurement techniques involving imaging by planar scintillation camera, SPECT and PET for the calculation of activity in source regions as a function of time are discussed. In addition, nonimaging measurement techniques, including external radiation monitoring, tissue-sample counting (blood and biopsy) and excreta counting are also considered. The third phase, data processing, involves curve-fitting techniques to integrate the source time-activity curves (determining the area under these curves). For some applications, compartmental modeling procedures may be used. Last, appendices are included that provide a table of symbols and definitions, a checklist for study protocol design, example formats for quantitative imaging protocols, temporal sam-

pling error analysis techniques and selected calculational examples. The utilization of the presented approach should aid in the standardization of protocol design for collecting kinetic data and in the calculation of absorbed dose estimates.

J Nucl Med 1999; 40:37S-61S

I. INTRODUCTION

The absorbed radiation dose from internally deposited radionuclides is a major factor in assessing risk and therapeutic utility when evaluating new radiopharmaceuticals for use in nuclear medicine diagnosis or treatment. Although direct measurements of absorbed dose and dose distributions in vivo would be preferable, this generally is not feasible for routine clinical studies. Absorbed dose, therefore, is a quantity that usually is estimated from the localized uptake and retention of administered radiopharmaceuticals, the radiation decay data of the radionuclide and simulations of radiation transport in anthropomorphic models. The measurement of the biodistribution of radiopharmaceuticals in human subjects and the use of these data in the Medical Internal Radiation Dose (MIRD) schema (1,2) provide a primary means for calculating absorbed dose from internally deposited radionuclides. Ultimately, it is desirable to correlate the absorbed dose calculated from such a model with the observed response for the tissue of interest (e.g., regression/ablation in the case of tumor and toxicity for critical organs). The radiation dose rate received from internal emitters is highly variable and is often delivered over a protracted time frame; consequently, the relation between absorbed dose and radiobiologic effect may not be inferred directly from the external beam experience (3). In this report, we review the MIRD schema, data acquisition methods, analysis and processing of biodistribution data from human subjects needed for calculations of radiation dose estimates. Through this approach to dosimetry, standardization of the calculation of absorbed dose estimates for diagnostic and therapeutic purposes may be achieved. It is hoped that this will ultimately lead to increasing success in identifying correlations between calculated absorbed doses from administrations of radiopharmaceuticals and the clinically observed effects.

Received Dec. 10, 1997; accepted Apr. 7, 1998.

For correspondence contact: Jeffrey A. Siegel, PhD, 216 Society Hill, Cherry Hill, NJ 08003.

This is the second of a series of MIRD Special Contributions.

The document has been prepared in a format to address two audiences:

1. Individuals with a primary interest in designing clinical trials who are not experts in dosimetry; and
2. Individuals with extensive experience with dosimetry-based protocols and calculational methodologies.

For the first group, the general concepts involved in data acquisition are presented with guidance provided for the number of measurements (data points) required. For those with expertise in dosimetry, highlighted sections (in boxed areas below), examples and appendices have been included to provide calculational details as well as references for the techniques involved. Appendix A provides a table of all symbols and definitions used in this document (Table A1). This document is intended also to serve as a guide for the investigator in choosing the appropriate methodologies when acquiring and preparing product data for review by national regulatory agencies.

The quantitative biologic data collection, analysis and processing schemes presented here will yield results that represent an average uniform distribution of activity within the source regions. Nonuniform distribution of the radionuclide is not considered. Bolch et al. (4), in the last issue of *The Journal of Nuclear Medicine*, provide a more comprehensive treatment of nonuniform activity distributions. The potentials of SPECT and PET technologies for quantitative data acquisition and analysis are discussed in brief; however, the intended emphasis of this document is on planar imaging techniques commonly available in most nuclear medicine departments and laboratories. Planar imaging systems, particularly dual-head whole-body scanners, provide both a cost- and time-effective method for acquiring data, as required for sequential dosimetry studies.

II. THE MIRD SCHEMA

An accurate determination of the time-dependent activity in tissues of the body is required for calculating absorbed dose to target regions of the body using the MIRD schema (1,2). In this document, the term "region" will be used to designate sources of radioactivity in the body and to designate targets for the assessment of radiation absorbed dose. Source regions should always be considered target regions as well; however, the dose to other target regions is usually of interest. In many cases, a source region will be synonymous with a source organ, such as the liver, or a distributed organ, such as the bone marrow. In some cases, however, the source region may be an organ subregion such as the caudate nucleus within the brain, or suborgan region of tissue (i.e., voxel).

The absorbed dose is defined as the energy absorbed per unit mass. The mean absorbed dose to tissue is given in the MIRD schema by $\bar{D} = \bar{A} \times S$, where \bar{D} is the mean absorbed dose (Gy or rad), \bar{A} is the cumulated activity (Bq · sec or $\mu\text{Ci} \cdot \text{hr}$) and S is the mean absorbed dose per unit cumulated activity (Gy/Bq · sec or rad/ $\mu\text{Ci} \cdot \text{hr}$). The absorbed dose to the target may also be expressed in terms of absorbed dose per unit administered activity, A_0 (Bq or μCi), and the source region residence time τ , defined as $\tau = \bar{A}/A_0$. Therefore, the mean dose to the target per unit administered activity is given by $\bar{D}/A_0 = \tau \times S$. The estimation of absorbed dose is, thus, dependent upon two types of information:

1. Time-dependent (biokinetic) factors: those incorporated within \bar{A} or τ ; and
2. Time-independent (physical) factors: those represented within S .

The time-dependent factor \bar{A} incorporates characteristics of both uptake and retention of activity in the regions of interest and includes consideration of the physical half-life of the radionuclide and the biologic half-time of the radiopharmaceutical. The time-independent factor S includes consideration of the types and energies of the radiations emitted, geometrical aspects such as the size and shape of the source and target regions and the distance between them and the composition of the absorbing and intervening media.

To determine the cumulated activity in the desired source regions, serial measurements of region activity must be made following administration of the radiopharmaceutical. A general principle for collecting activity data in vivo is that quantitative procedures or calculations must account for all the activity administered. A minimum number of quantitative measurements must be made for each source region with an appropriate temporal sampling frequency. The latter depends upon the pattern of the uptake and retention of the activity in the various source regions. Serial measurements of activity in the source regions can be performed using quantitative imaging (including planar scintillation camera, SPECT or PET), external nonimaging radiation monitoring, tissue sampling (blood or biopsy) and excreta counting. Total-body retention may be determined using whole-body quantitative imaging, external probe monitoring (nonimaging) and/or quantitative total recovery of body excreta. Activity in blood is readily obtained by direct sampling. The resulting time-activity curve obtained for each source region can be analyzed using several different techniques to provide \bar{A} or τ , for use in absorbed dose calculations.

This report describes data acquisition protocols that may be implemented to obtain source region activities and how these data are analyzed and processed to estimate absorbed radiation dose using the MIRD schema (a study design protocol checklist is given in Appendix B). Three phases are involved:

1. Data collection: identification of the various source regions containing activity, determination of appropriate temporal sampling and acquisition of radioactivity or count data;
2. Data analysis: calculation of activity in source regions as a function of time using the count data and calibration factors obtained from quantitative measurement techniques; and
3. Data processing: integration of the time-activity curves to obtain the sum of all the nuclear transitions, cumulated activity \bar{A} or residence time τ in each source region.

These three phases are described below in detail.

III. DATA COLLECTION

A. Introduction

To determine the time-activity profile of the radioactivity in source regions, four questions must be answered:

1. What regions are source regions?
2. How fast does the radioactivity accumulate in these source regions?
3. How long does the activity remain in the source regions? and
4. How much activity is in the source regions?

The first question concerns identification of the source regions, whereas the second and third questions relate to the appropriate number of measurements to be made in the source regions, as well as the timing of these measurements. The fourth question is addressed through quantitative external counting and/or sampling of tissues and excreta.

Each source region must be identified, and its uptake and retention of activity as a function of time must be determined. This provides the data required to calculate cumulated activity or residence time in all source regions. Each region exhibiting significant radionuclide uptake should be evaluated directly where possible. The remainder of the body (total body minus the source regions) must usually be considered as a potential source as well. Mathematical models that describe the kinetic processes of a particular agent may be used to predict its behavior in regions where direct measurements are not possible but where sufficient independent knowledge about the physiology of the region is available to specify its interrelationship with the regions or tissues in which uptake and retention can be measured directly. These models can account for the presence of metabolic products. Compartmental modeling can also be used to separate the activities in regions that overlap on imaging studies, such as the renal cortex and renal pelvis or the liver and right colon. Some compartmental models are complex and include compartments representing many different biologic processes. Several computer software packages (SAAM, CON-SAM, BMDP and so on) are available to solve the equations associated with the different compartmental models (5–7).

The statistical foundation of a data acquisition protocol designed for dosimetry requires that an adequate number of data points be obtained and that the timing of these points be carefully selected. As the number of measurements increases, the confidence in the fit to the data and in the estimates of unknown parameters in the model improves. As a heuristic or general rule of thumb, at least as many data points should be obtained as the number of initially unknown variables in the mathematical curve-fitting function(s) or in the compartmental model applied to the data set. For example, each exponential term in a multiexponential curve-fitting function requires two data points to be adequately characterized. On the other hand, if it is known a priori that the activity retention in a region can be accurately represented by a monoexponential function, restrictions on sampling times are less stringent as long as enough data points are obtained to derive the fitted function. Because of problems inherent in the collection of patient data (e.g., patient motion, loss of specimen and so on), the collection of data above the necessary minimum is advisable.

B. Identification of Source Regions

The types of measurements required for identifying source regions can be categorized into four basic groups: imaging, discrete probe monitoring (whole-body or region counting), tissue sample (blood or biopsy) counting and excreta counting. Published literature on humans or animal studies along with *ex vivo* or *in vitro* data may yield valuable information to assist in identifying tissues that accumulate a particular radiopharmaceutical. This information, if available, may serve as the basis for designing the preliminary data acquisition protocol.

The distribution of a radiopharmaceutical in the body can be determined by sequential imaging methods. Quantitative data can be obtained from planar scintillation camera images or tomographic SPECT or PET images (example quantitative imaging protocols are given in Appendix C). Because of the time-consuming and more complex nature of quantifying SPECT and PET tomographic image data, conjugate view quantitative planar imaging, using anterior and posterior views, is the most widely used method (8,9) and will be emphasized in this report. The whole-body imaging capability of current single- and dual-head scintillation cameras is especially useful for this purpose. Total-body measurements may also be obtained with an external nonimaging radiation probe. In addition,

source regions can be identified by tissue and excreta sampling. All measurements must provide quantitative results in terms of absolute activity (Bq) or percent or fraction of administered activity within source regions. Counts or count rates uncorrected for administered activity are inadequate for the quantitative analysis required in dose estimate calculations.

For determining source region volume, especially for tumors or regions of abnormal size where standard phantom geometries may be inadequate, the tomographic capability of SPECT or PET may be required. Independent imaging modalities such as x-ray CT or MRI may also be used for source volume determination, provided a one-to-one correspondence exists between uptake and anatomic structure.

C. Temporal Sampling

After the source regions have been identified, the activity retention in these regions must be determined to answer the following questions: How fast does the activity get to the various source regions? How long does the activity stay there? The calculation of absorbed dose requires that the region and total-body uptake, washout and long-term retention be characterized. Four basic kinetic models are considered here (calculational examples are given in Appendix E):

1. Instantaneous uptake (wash-in) with no biologic removal;
2. Instantaneous uptake with removal by both physical decay and biologic elimination (washout);
3. Noninstantaneous uptake with no biologic removal; and
4. Noninstantaneous uptake with removal by both physical decay and biologic elimination.

Selection of optimal time points for sampling radiopharmaceutical biodistributions in humans with the objective of defining the uptake and retention pattern is dependent upon the biokinetic variables to be measured, e.g., effective half-times. Relevant quantitative data for similar radiopharmaceuticals obtained in animal or human trials may serve as a guide for the initial choice of these time points. The selection of the sampling times can have a significant effect on parameter estimation precision (10). Readers interested in pharmacokinetics may refer to Appendix D for a rigorous mathematical treatment of the statistical consequence of applying inappropriate temporal sampling.

As a practical guide for those who are designing clinical trials with new radiopharmaceuticals, consideration should be given to which one of the following three general categories most closely describes the experimental status of the new compound (11):

- Category 1. Radiopharmaceutical compounds for which neither *in vivo* animal studies nor human pharmacokinetic clinical trials have been conducted. Included also in this category are those compounds for which pertinent information is limited to general chemical and biologic class comparison (e.g., antibody fragments with a chelated metal, single-chain haptens undergoing a standard iodination procedure and so on). The labeled compound should be injected into at least two animal species, as per Food and Drug Administration (FDA) guidelines (12) to determine the uptake and retention characteristics in all source regions prior to administration in human subjects. As a starting point, pharmacokinetic temporal sampling points may be selected based on the physical half-life (T) of the radionuclide or the effective half-time (T_e) of

the pharmaceutical compound in the blood or source region of interest (ROI). A minimum of three sampling points should be chosen for each clearance exponential, if known or suspected. A general protocol could involve one or two data points taken at some fraction of T_e ; one near T_e ; and one or two other data points taken at $\sim 3 \times T_e$ and $5 \times T_e$. Data points can serve for more than one exponential. If nothing is known about the retention of the compound in animals and humans, multiple sampling times, say a dozen, should provide a reasonable starting point. Insufficient data points may make it impossible to properly characterize a multicompartmental model, thereby resulting in patient irradiation to little purpose. As an alternative, an estimate of sampling times may be based on the molecular weight and size of the compound as well its ionization potential or charge as compared to similar compounds in the literature.

Category 2. Radiopharmaceutical compounds for which the biodistribution has been characterized in at least two animal species and some preliminary pharmacokinetic data have been acquired in a patient study (5–20 normal volunteers or patients with known disease). Extensive literature on this compound or similar analogs should be available. The investigator should be able to project a reasonable hypothesis as to whether clearance parameters are mono- or biexponential or more complicated because of retention and excretion from multiple specific uptake compartments. Again, at least three sampling points should be taken for each exponential, based on T_e in the blood or source region of interest in either animals or humans.

Category 3. Radiopharmaceutical compounds for which all pertinent literature related to the pharmacokinetics of similar labeled compounds has been compiled, and extensive animal model and human pharmacokinetic data have been acquired. The compound has most likely completed Phase I and Phase II clinical trials. Uptake should be characterized in all the source regions for the animal models and in the human subjects. Remainder of the body and blood retention, as well as urinary excretion characteristics, should be known. From these data, a cost-effective, highly directed Phase III clinical trial may be designed.

Radiopharmaceuticals that show rapid uptake or washout may need two or three activity measurements at early times postadministration. Radiopharmaceuticals that show very rapid uptake may require no wash-in measurements. Similarly, two, three or more additional data points may be required during the long-term retention phase to adequately characterize the late time course of the radiolabeled material. Where the presence of disease may alter region function, the acquisition of additional data in the affected tissues may be advisable.

From serial activity measurements, one can determine the residence time defined as the area under the time–activity curve (i.e., cumulated activity \bar{A}) divided by the administered activity A_0 . Errors in estimates of \bar{A} and thus in the residence time may be introduced as a result of improper sample timing and an inadequate number of samples when analytical functions are

used to approximate the measured time–activity curve. Because many processes in the body are governed by first-order kinetics, sums of exponentials are often used as these mathematical functions. As illustrated in Appendix D, the number of measurements needed is directly related to the number of exponential terms in the retention curve. Ideally, two to three measurements per exponential term are required. Therefore, if the total-body clearance curve is a single exponential, three data points are needed. A biexponential retention curve would require a minimum of four and preferably six data points and so on. When the distribution of samples is appropriately spread over the time interval for which activity is taken up and removed, then the mathematically simulated curve is an accurate representation of the time–activity profile. However, restrictions on the timing or number of samples may necessitate extrapolation of the simulated curve to time intervals for which no data exist. These intervals extend from $t = 0$ (the time of radiopharmaceutical administration) to the first sample and from the last sample point to very long times postadministration, i.e., to the total clearance time of the compound.

For further refinement, both the uptake phase and the washout phase must be characterized accurately. The uptake phase is the period over which the region activity increases from zero (at the time of administration) to its maximum value. Answers to the following questions will characterize this phase: Was the uptake slow or fast (qualitative information)? What was the uptake half-time (relevant if curve fitting)? What was the fractional uptake in the region? If a compartmental model was used, were there any special parameters necessary to describe the uptake phase? The duration of the uptake phase in a given region may vary widely with different radiopharmaceuticals. It is often assumed that uptake of the radiopharmaceutical is instantaneous (i.e., the peak uptake occurs immediately following administration); however, in many cases this is inaccurate. Errors generated by this assumption will result in an overestimate of the source region residence time and thus an overestimate of the dose component from that source to various targets. The instantaneous uptake assumption may be considered satisfied when extrapolation of the observed data back to $t = 0$ results in less than a 10% error in the residence time as compared to the residence time estimated from a curve fit that accurately reflects the noninstantaneous uptake phase.

The washout (clearance) phase is the period over which the activity retained in a region decreases from its maximum value. In addition to physical decay, biologic elimination may also occur, making the effective washout time more rapid than physical decay alone. This portion of the curve will also affect the \bar{A} calculation (area under the curve) independent of the uptake phase. For example, if the uptake phase is ignored (i.e., by extrapolating the linear portion of the semilog time–activity curve back to time 0 and integrating the area under the extrapolated curve), the overestimation of area under the curve will be greater for faster washout conditions. Therefore, if rapid washout occurs, as is typical of freely diffusible ions (such as $^{18}\text{F}^-$ and $^{201}\text{Tl}^+$), data must be acquired at early times postadministration of the radiopharmaceutical.

To characterize the long-term retention (tissue incorporation or trapping of the radiopharmaceutical), measurements at times equal to multiples (2–5) of the effective half-time are needed. Frequently, this may be accomplished within several hours postadministration; however, measurements are more often required at much later time points. If the data acquisition ends too early, the area under the curve would not be representative of that under the true retention curve because the long-term retention phase would not be included. Because the late

retention is usually characterized by the longest effective half-times, the calculated area under the curve would typically be an underestimate. Large errors can result in residence time calculations if the long-term retention phase is ignored. For example, if the ratio of the effective washout half-times of the slow-to-rapid clearing components is 4:1 or greater, the errors start at 30% and rapidly increase to 100% (see Appendix D).

The physical half-life of the radionuclide plays an important role in determining the period over which reliable data may be obtained. After approximately five half-lives, count statistics can be extremely poor, and the data may be less reliable. Under these conditions, counting times should be increased, if possible, to maintain adequate statistical reliability.

In summary, improper sampling may introduce error in calculated values of \bar{A} (and thus residence time) under conditions that neglect uptake, early rapid washout or the long-term retention component. The first two conditions relate to insufficient sampling of tissue activity at times just after administration and will result in an overestimation of the area under the time-activity curve. The loss of activity from the source region can occur in one of two ways: physical decay only or physical decay plus biologic elimination. Clearly, if biologic processes are contributing to removal of activity from the source region, the residence time for that region will be less than if losses are due to physical decay only. When instantaneous uptake is assumed, the peak uptake (at time 0) is determined by extrapolation back to $t = 0$ based on the data measured at later times. The extrapolation process results in greater overestimates of the peak uptake as the rate of biologic removal increases. The major implication of overestimating peak uptake and not accounting for noninstantaneous uptake is an overestimate of the residence time for that particular source region. The third condition (neglect of the long-term retention), resulting from insufficient sampling at times long after administration, will result in an underestimate of the residence time. Error analyses associated with these considerations are discussed in Appendix D.

D. Data Acquisition Concepts/Overview

The acquisition of count data for the source regions can be performed with a number of measurement techniques. They include:

1. Quantitative imaging, with a planar scintillation camera or tomographic SPECT or PET system;
2. External nonimaging radiation monitoring with a NaI probe or GM survey meter;
3. Tissue sample counting of the blood or biopsy specimen; and
4. Excreta counting (e.g., urine and feces).

The technique used depends on the nature of the source region. For instance, the total-body activity can be measured by whole-body monitoring with a nonimaging device, whole-body imaging or stationary counting with a scintillation camera or quantitative recovery of body excretions. Individual tissue activity can be determined by quantitative imaging, blood sampling and biopsy specimen measurement.

IV. QUANTITATIVE MEASUREMENT TECHNIQUES: IMAGING

A. Scintillation Camera Planar Imaging Techniques

1. Introduction

A number of factors affect the accuracy of quantitating radioactivity with a scintillation camera. These include limitations on energy resolution, degradation of spatial resolution due to collimator septal penetration by high-energy photons and

effects from scattered radiation, statistical noise associated with low count densities and attenuation. The spatial resolution in planar images depends upon the intrinsic resolution of the NaI(Tl) scintillation crystal, the collimator and Compton scatter. The collimator also plays the important role of defining geometric sensitivity (the fraction of emitted photons per unit time which reach the crystal from a predefined location/direction). Parallel-hole collimators are recommended for quantitation of radioactivity because they exhibit less geometric distortion when compared to other types of collimators (e.g., converging, pinhole and diverging), with the result that sensitivity will be relatively independent of source-to-collimator distance within a defined region. Spatial resolution of a scintillation camera degrades, however, as the distance between the source and the detector increases. Consequently, the detector should be as close as possible to the subject.

Biodistribution (kinetic) data for radiopharmaceuticals within the whole body and specific regions may be obtained from planar scintillation camera views. The accuracy of this method will be greatest for radiopharmaceuticals distributed in a single region or isolated regions that do not overlap (nonsuperimposed) in the planar projection. Determination of absolute radioactivity requires definition of ROIs corresponding to the source regions as differentiated from their adjacent or surrounding background activity. Most scintillation camera systems used in clinical nuclear medicine are computer-based and provide software for generation of ROIs and statistical analysis. Commercial software packages typically provide the means for creating ROIs of simple geometry (circles, ellipses and rectangles) and for interactive drawing of irregularly shaped ROIs. This latter capability is important for determining activity in regions that cannot be described by simple geometries such as most source regions and tumors. Automated or semiautomated methods for ROI generation are also available. Statistical analysis packages provided with these commercial systems allow determination of the number of pixels contained within the ROI, the planar area encompassed, the total number of counts and the mean and s.d. of the counts per pixel. The count rate within the ROI is obtained from the total number of counts divided by the image acquisition time. Sequential imaging as a function of time postadministration of the radiopharmaceutical provides the time dependence of activity (time-activity curve) within the source regions. Generally, the computer software packages permit storage of the ROIs, allowing reproducible, efficient analysis of serial image data.

2. Conjugate View Counting

An overview of the methodology. The most commonly employed imaging method for quantitation of radioactivity in vivo uses 180° opposed planar images (known as the conjugate view approach) in combination with transmission data through the subject and a system calibration factor (9,13-16). This technique offers an improvement over the single-view procedures involving comparison with a standard phantom under fixed geometry in that the rigorous mathematical formalism for conjugate view quantitation provides correction for source thickness, inhomogeneity and attenuation. Of significance is the fact that calculational results are theoretically independent of the source depth in tissue. The transmission scan, which involves counting an external source of activity through the source ROI to correct for attenuation, is generally performed at one time point, either at the beginning of the study before the administration of the radiopharmaceutical or at a later time with appropriate correction made for activity in the body.

The conjugate-view image pair is typically an anterior and

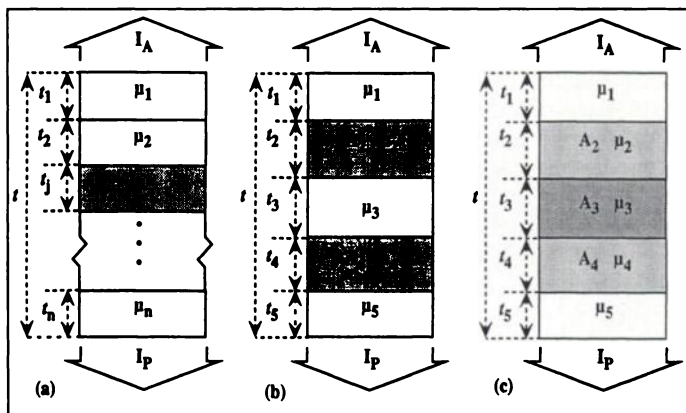


FIGURE 1. Schematic diagrams for various configurations of source regions within tissue zones of differing attenuation coefficients. All symbols are defined in the text (see also Table A1). The shaded areas denote the regions of activity. (a) A single uniform source region embedded in a medium consisting of n zones of differing attenuation coefficients. (b) Two regions of uniform activity embedded in attenuating medium with region 2 considered as the primary source for quantitation. (c) Uniform background activity in tissue regions surrounding the primary source. Adapted from a previous report (9).

posterior (A/P) image of the source region, although any true 180° opposed set might be used (e.g., right and left lateral). This conjugate image pair is acquired at the selected sampling times postadministration for which quantitative data are desired; in cases in which source region activity is not time-dependent, a single conjugate-view measurement may be adequate (see Appendix C). Modern dual-headed scintillation cameras provide a convenient means for simultaneous acquisition of the two images and commonly allow capability for whole-body A/P scans. The latter represents an efficient protocol for obtaining total-body data as required for biodistribution studies. However, single-head camera systems may be used with repositioning and reimaging as necessary to obtain the conjugate view. The system calibration factor is required to convert the source region count rate into absolute activity. The calibration factor should be measured at each acquisition time point to document that the system response remains constant or to account for any change in performance that might affect the observed count rate.

Mathematical formulation of the conjugate view method.

a. Discrete Source Regions with Negligible Surrounding Background Activity. *i. Isolated Single Source Region.* Figure 1a depicts a single uniform source of thickness, t_j (cm), embedded in a nonradioactive medium consisting of n regions of thickness, t_n , with differing linear attenuation coefficients, μ_n (cm^{-1}) (9,16). The external conjugate-view counting pair (A/P) across the overall patient thickness t is shown as I_A and I_P (counts/time). The derivation assumes that the views are perfectly collimated under the model of narrow-beam geometry without significant scattered radiation effects. These conditions may be achieved in practice through use of a high-resolution collimator and a narrow or asymmetrically positioned photopeak energy window on the scintillation camera. (Methods for implementing scatter correction are discussed in other sections below.)

The source activity A_j is given by the expression:

$$A_j = \sqrt{\frac{I_A I_P}{e^{-\mu_e t} C}} f_j \quad \text{Eq. 1}$$

where:

$$f_j \equiv \frac{(\mu_j t_j / 2)}{\sinh(\mu_j t_j / 2)} \quad \text{Eq. 2}$$

and

$$\mu_e = (1/t) \sum_{i=1}^n \mu_i t_i = \mu_j + (1/t) \sum_{i=1}^n (\mu_i - \mu_j) t_i \quad \text{Eq. 3}$$

The factor f_j represents a correction for the source region attenuation coefficient (μ_j) and source thickness (t_j) (i.e., source self-attenuation correction). The expression $e^{-\mu_e t}$ represents the transmission factor (\mathcal{T}) across the patient thickness t through the ROI with overall effective linear attenuation coefficient μ_e and may be determined directly by measuring the ratio of the count rates I/I_0 , obtained using the appropriate radioisotope both with (I) and without (I_0) the patient in position. The system calibration factor C (count rate per unit activity) is obtained by counting a known activity for a fixed period of time within a standardized geometry in air relative to the scintillation camera using designated camera acquisition settings.

The conjugate view technique allows determination of activity within the volume of interest without requiring knowledge of the depth of the source region and without dependence upon assumptions inherent in single-view phantom simulations. The factor f_j (≤ 1.0) involves only the source region characteristics and will not deviate significantly from 1.0 until μ_j or t_j becomes large. The thickness of an organ may be estimated by acquiring a scaled orthogonal view (e.g., a lateral image) and taking direct measurements from the image.

ii. Overlapping Source Regions. A specific configuration of interest is shown in Figure 1b involving two separate regions of uniform activity embedded within tissue containing no radioactivity such that the regions overlap in the conjugate view projection. The expression for the activity in source volume 2 is:

$$A_2 = \sqrt{\frac{I_A I_P}{e^{-\mu_e t} C}} f_2 g(\alpha), \quad \text{Eq. 4}$$

where:

$$g(\alpha) \equiv \{1 + (\alpha f_2 / f_4)^2 + 2\alpha(f_2 / f_4) \cosh[(\mu_2 t_2 + 2\mu_3 t_3 + \mu_4 t_4) / 2]\}^{-1/2} \quad \text{Eq. 5}$$

Once again, the f -factors are defined through Equation 2, while $\alpha \equiv A_4 / A_2$ is the ratio of the activities in the two regions. Additional views would be used to estimate the various parameters (t_j and α).

b. Background Subtraction: A Single Well-Defined Source Region Surrounded by Regions of Background Activity.

i. Simple Background Subtraction. In practice, the primary source is frequently surrounded by radioactivity residing in adjacent tissues (Fig. 2). This so-called "background" activity may arise from radionuclide concentration in blood, extracellular fluid or soft tissue. Utilization of conjugate view data to determine the absolute activity in the source volume according to the analytical method described in Equation 1 would overestimate the activity because the overlying and underlying background activity contribute counts to each view. Conventional background subtraction, i.e., subtraction of the background count rate from the source region count rate, does not

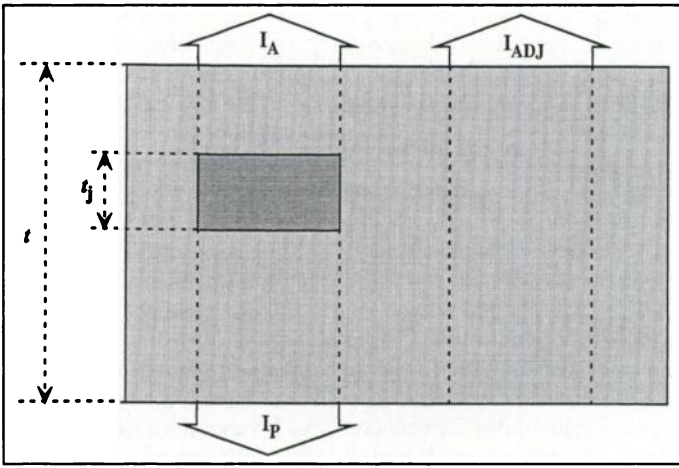


FIGURE 2. A schematic diagram showing a single source region surrounded by uniform background activity. As described in the text, the count rate from an adjacent, equal-sized ROI (I_{ADJ}) may be used in a simple background subtraction method to correct the conjugate-view count rates for the contribution of the over/underlying activity.

consider the portion of the background equivalent to the source region volume and may underestimate the source region activity due to oversubtraction of background (17). In addition, defining background ROIs is sometimes difficult as care must be taken to avoid hot or cold areas, such as major blood vessels.

A simple geometrically based subtraction technique may be applied to correct for the oversubtraction of background activity and to avoid the problems inherent in background ROI definition. Under conditions in which the background activity is uniform, the fraction of the geometric mean counts ($I_A I_P$)^{1/2} that originates from the region (or volume) of interest alone is given as:

$$F = \left\{ \left[1 - (I_{ADJ}/I_A)(1 - t_j/t) \right] \left[1 - (I_{ADJ}/I_P)(1 - t_j/t) \right] \right\}^{1/2}, \quad \text{Eq. 6}$$

where I_{ADJ} is the count rate through the patient from a region adjacent to the organ ROI with equal area. The A/P count rates (I_A/I_P), source thickness (t_j) and patient thickness (t) remain as previously defined. Direct patient measurement will provide t , and t_j may be obtained from scaled lateral views or through use of standard organ dimensions as appropriate (18,19). The lateral view may also be used to document the assumption of uniform background activity distribution. For the situation in which the source is located near the midline, a simplified expression for this fraction is:

$$F \cong \left[1 - (I_{ADJ}/I_A)(1 - t_j/t) \right]. \quad \text{Eq. 7}$$

In either case, $F(I_A I_P)^{1/2}$ would replace $(I_A I_P)^{1/2}$ in Equation 1.

ii. Analytical Methodology. Figure 1c illustrates the situation in which a well-defined source is surrounded by background activity uniformly distributed in the adjacent tissue. For this configuration, the source region activity A_3 is given by the expression:

$$A_3 = \sqrt{\frac{I_A I_P}{e^{-\mu_a t}} \frac{f_3}{C}} k(\gamma), \quad \text{Eq. 8}$$

where

$$k(\gamma) \equiv \left\{ 1 + (\gamma_2 f_3/f_2)^2 + (\gamma_4 f_3/f_4)^2 + 2\gamma_2 \gamma_4 (f_3^2/f_2 f_4) \cosh [(\mu_2 t_2 + 2\mu_3 t_3 + \mu_4 t_4)/2] + 2\gamma_2 f_3/f_2 \cosh [(\mu_2 t_2 + \mu_3 t_3)/2] + 2\gamma_4 f_3/f_4 \cosh [(\mu_3 t_3 + \mu_4 t_4)/2] \right\}^{-1/2}. \quad \text{Eq. 9}$$

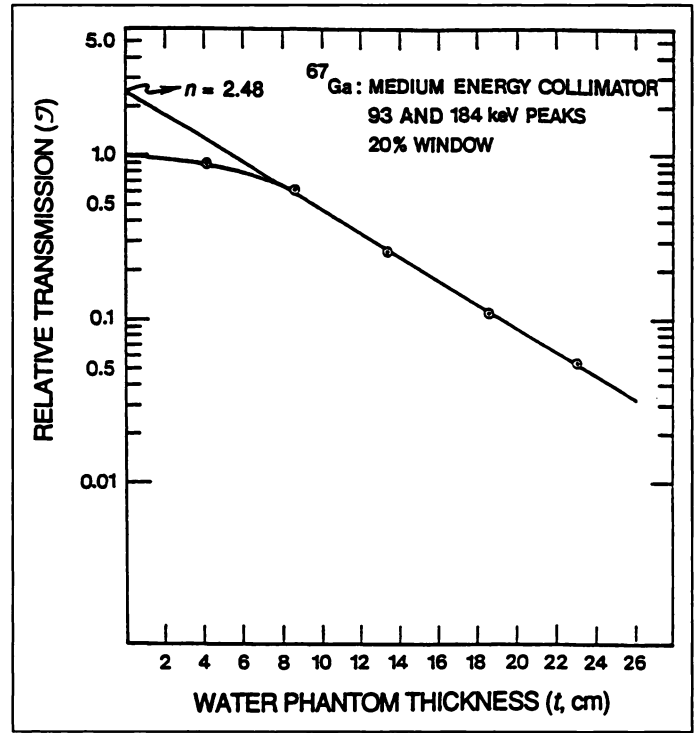


FIGURE 3. An experimentally measured transmission curve in a tissue equivalent medium for the two photopeaks of ⁶⁷Ga using a medium-energy collimator. The curve exhibits a significant shoulder characteristic of scattered radiation effects which requires use of the pseudoextrapolation number modification of the conjugate view quantitation equations. For $t \geq 6$ cm, $\mathcal{T} = ne^{-\mu_a t}$ and the activity is calculated according to Equation 10. Adapted from a previous report (20).

The individual f factors are defined according to Equation 2, whereas $\gamma_2 \equiv A_2/A_3$ and $\gamma_4 \equiv A_4/A_3$ represent the ratios of the activity in the adjacent regions to that in the source volume. Calculation of the $k(\gamma)$ constant requires estimates of the factors (f_j , γ_2 , γ_4) that may be obtained through analysis of additional views in combination with the main conjugate view pair. The $k(\gamma)$ correction may become significant when the activity in the adjacent regions approaches 10% of that in the source volume (9,16).

c. Correction for Scattered Photons. As stated, the above analytical methods (Eqs. 1–9) have been derived under the model of narrow-beam geometry in which scatter effects are negligible. The investigator must verify that these conditions are met for his/her experimental data acquisition configuration before applying these methods. High-resolution collimators and narrow, asymmetric energy window settings assist in approximating these conditions. However, in most nuclear medicine imaging applications, broad-beam geometry predominates and scatter effects are significant. The presence of scattered photons originating from outside the source organ ROI will artificially inflate the ROI count density and introduce error in the quantitation of radioactivity. The following sections describe a number of approaches designed to correct for scatter.

i. Pseudoextrapolation Number. An illustration of the effect of scattered radiation is provided in Figure 3, where the curve for the relative transmission (\mathcal{T}) as a function of depth within a scattering medium exhibits a shoulder on the semilog plot rather than the straight line expected from the simple narrow beam model for transmission of $\mathcal{T} = I/I_0 = e^{-\mu_a t}$. The shoulder is a manifestation of increased count density within the ROI caused by acceptance of scattered photons from activity close to the

collimator. A modified expression to account for this situation has been developed by Thomas et al. (20) in which the intercept n is thought of as a pseudo-extrapolation number (following the terminology used with radiobiology survival curves). For the straight line portion of the semilog plot of Figure 3, $\mathcal{T} = ne^{-\mu_0 t}$ where μ_0 is the equivalent narrow-beam geometry linear attenuation coefficient. For a single-source region embedded within a scattering medium with no surrounding background activity, the modified expression for the source activity would be:

$$A_j = \sqrt{\frac{I_A I_P}{n \mathcal{T} C}} f_j \quad \text{Eq. 10}$$

This is valid for source regions located at depths beyond the transmission curve shoulder corresponding to the straight line portion of the plot.

ii. *Buildup Factor Method.* Another approach to the scattering problem has been described by Wu and Siegel (21). Their method employs conjugate views and experimentally determined depth-dependent buildup factors (DDBF) which are defined as the factor by which the transmission is increased under broad-beam (scatter) conditions. No transmission measurement is made across the patient. An iterative calculational procedure is used involving the solution of the set of simultaneous equations representing the conjugate-view count rate pairs.

$$I_A = C_{od} B(d) e^{-\mu d} [e^{-\mu t/2} (1 - e^{-\mu t}) / \mu t_j] \\ = C_{od} B(d) e^{-\mu d} [\sinh(\mu t_j/2) / (\mu t_j/2)] \quad \text{Eq. 11}$$

and

$$I_P = C_{od} B(t-d) e^{-\mu(t-d)} [e^{-\mu t/2} (1 - e^{-\mu t}) / \mu t_j] \\ = C_{od} B(t-d) e^{-\mu(t-d)} [\sinh(\mu t_j/2) / (\mu t_j/2)], \quad \text{Eq. 12}$$

with the depth-dependent buildup factor $B(d)$ defined as

$$B(d) = \frac{C_d}{C_{od} e^{\mu d}}, \quad \text{Eq. 13}$$

where C_d is the count rate measured at a depth d at the center of the lesion in a phantom, C_{od} is the count rate measured in air at the same source-to-gamma camera distance, μ is the attenuation coefficient, t is the overall patient thickness and t_j is the source thickness.

The depth-dependent buildup factors $B(d)$ must be determined from experimental measurements and depend upon the radionuclide, collimator type, energy window, measurement geometry, source depth, source size and source thickness. The $B(d)$ values are stored in the computer memory as specific tables to be used in association with the appropriate system conditions. The equation set (Eqs. 11 and 12) are solved iteratively for C_{od} and d under the initial assumption that the source is located exactly at the center by using $B(t/2)$ in both expressions. This initial calculated value of d is used to select buildup factors $B(d)$ and $B(t-d)$ from the look-up table for the second iteration and new values for C_{od} and d are calculated. This iterative procedure continues until a solution for C_{od} converges. The activity is then determined by $A_j = C_{od}/C$, where C (count rate per unit activity) is the system calibration factor.

As pointed out by Wu and Siegel (21), the pseudoextrapolation number modification method of Thomas et al. (20) is equivalent by definition to the buildup factor at depths corre-

sponding to the straight-line portion of the transmission curve (Figure 3). As described previously, the parameter n is taken as a constant; therefore, Eq. 10 will not be valid for regions near the surface (i.e., in the shoulder of the curve). The DDBF with its variable, experimentally determined look-up table will include compensation for this effect. The DDBF technique requires a more complicated protocol of calibration set-up procedures and calculational algorithms than does the transmission method of Thomas et al. (9); however, it would have its greatest utility under conditions of significant scatter effects such as those encountered with wide windows and high-sensitivity collimators. The investigator may determine the necessity of following this procedure by obtaining a transmission curve similar to that in Figure 3 under the appropriate instrumental conditions and assessing the extent of the shoulder region. To implement the buildup factor algorithms, a computer program may be written requiring only four input parameters (I_A , I_P , t and C) to calculate the activity.

A variation on the buildup factor theme has been introduced by Siegel et al. (22,23) involving a depth-independent buildup factor (DIBF). The DIBF method is easier to apply than the DDBF method in that only the single parameter $B(\infty)$ is required which is independent of source size and depth for a given window setting (23). The utility of the DIBF approach has been verified by a number of investigators (17,24).

In the DIBF method, the transmission factor \mathcal{T} as a function of depth d in tissue equivalent material with linear attenuation coefficient μ is fit to the function:

$$\mathcal{T} = 1 - (1 - e^{-\mu d})^{B(\infty)}, \quad \text{Eq. 14}$$

where $B(\infty)$ is the buildup factor at infinite depth (corresponding to the straight line portion of Fig. 3 and equivalent to the pseudoextrapolation number n previously discussed). The expressions for the experimentally measured conjugate view count rate pairs are:

$$I_A = C_{od} [1 - (1 - e^{-\mu d})^{B(\infty)}] [\sinh(\mu t_j/2) / (\mu t_j/2)] \quad \text{Eq. 15}$$

and

$$I_P = C_{od} [1 - (1 - e^{-\mu(t-d)})^{B(\infty)}] [\sinh(\mu t_j/2) / (\mu t_j/2)]. \quad \text{Eq. 16}$$

Equations 15 and 16 may be combined to give the ratio:

$$I_A/I_P = \frac{[1 - (1 - e^{-\mu d})^{B(\infty)}]}{[1 - (1 - e^{-\mu(t-d)})^{B(\infty)}]}, \quad \text{Eq. 17}$$

which may be solved numerically for d by varying the value of d under the constraint $0 \leq d \leq t$. Either Equation 15 or 16 may be used to calculate C_{od} from which the activity may be calculated through use of the calibration factor. Alternatively, if the anterior depth d is measured, C_{od} may be calculated from the expression for I_A (Eq. 15).

iii. *Multiple-Energy Window Techniques.* As already indicated, use of an asymmetric energy window positioned on the high side of the photopeak will decrease the amount of scattered radiation accepted from Compton scattering of the primary (photopeak) photons. However, the number of counts per unit time will be reduced, thus lowering the signal-to-noise ratio (25,26). In addition, scatter from higher-energy photons present in the specific radionuclide decay scheme will still be included within the window.

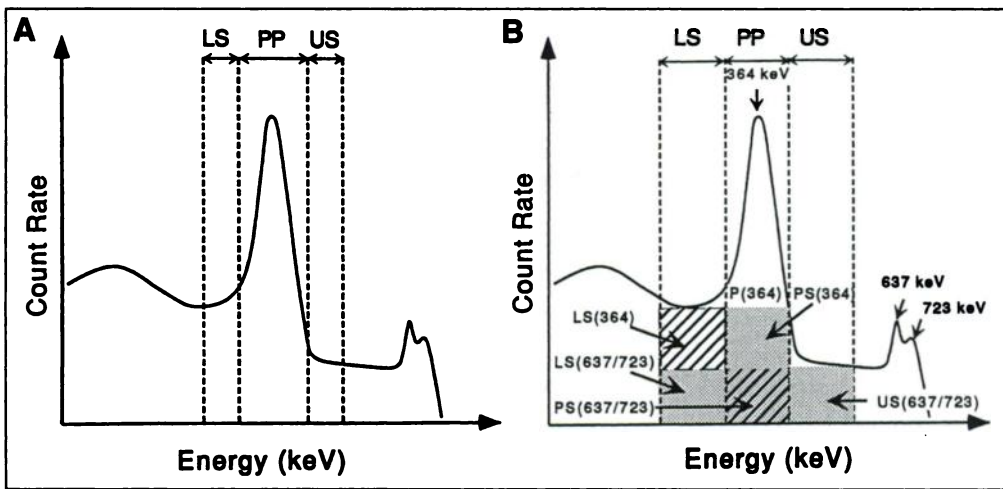


FIGURE 4. Triple-energy window (TEW) techniques. (a) A relatively simple triple-window correction involves placement of equal adjacent windows on the lower (LS) and upper (US) side of the photopeak (PP). The width of each of these windows is one-half that of the width of the photopeak (PP). Subtraction of the counts in these adjacent windows from the total counts within PP compensates for the high-energy photon scatter tail upon which the true photopeak events ride (18). (b) A somewhat more rigorous approach as applied specifically to ^{131}I is illustrated which involves definition of six components within the three energy windows. As described in the text, three scatter multipliers are derived which allow determination of the true photopeak events, P(363). Adapted from a previous report (30).

Some methods of explicit scatter correction using multiple-energy windows have been implemented using planar imaging. One such method, called the channel ratio (CR) method, uses two narrow adjacent windows centered over the photopeak (27). Data acquisition is similar to that employed by other investigators using dual energy windows (28); however, the data processing algorithm is distinctly different and does not involve scatter image subtraction. In brief, the CR methodology corrects the counts measured in the respective windows with scatter present on an individual pixel basis using empirically determined constants specific for the given scintillation camera and photon energy. These constants represent the ratio of counts in the two windows excluding scatter (theoretically 1.0; however, it may vary as a function of position on the camera face) and the ratio of the scatter component in the two windows (under the assumption that the relative shape of the scattered photon energy spectrum remains constant). Calibration is performed using a two-step process:

1. The fraction of unscattered counts in one window compared to the other is found for a small source that is essentially scatter-free; and
2. A sequence of planar images is acquired for a flat source placed at various depths in a nonradioactive water bath.

Triple-energy window (TEW) techniques were introduced for SPECT (29) but can be implemented for conjugate planar views to provide a more accurate correction in the situation when scatter from higher-energy photons “spills down” into the primary photopeak window. An example of this is ^{131}I , where the 637-keV (7.3%) and 723-keV (1.8%) photons scatter into the 364-keV (81%) window. One relatively straightforward correction procedure involves establishing adjacent windows on either side of the photopeak window, such that the area of the two similar adjacent windows is equal to that of the photopeak (Fig. 4a). The corrected (true) photopeak counts C_T are given by the expression:

$$C_T = C_{PP} - C_{LS} - C_{US}, \quad \text{Eq. 18}$$

where C_{PP} is the total count recorded within the photopeak window, whereas C_{LS} and C_{US} are the counts within the lower and upper scatter windows, respectively. In this model, subtraction of the adjacent windows is assumed to compensate for the high-energy photon scatter tail, upon which the true photopeak events ride.

A somewhat more rigorous variation of this method has been applied to conjugate views and entails definition of six separate components within the three windows (30). As shown schematically in Figure 4b for the specific case of ^{131}I , LS(637/723), PS(637/723) and US(637/723) are scatter and septal penetration contributions from the 637-keV and 723-keV photons in each of the respective energy windows; LS(364) and PS(364) are scatter contributions from the 364-keV photons that fall into the lower and photopeak windows, respectively; and P(364) are the true photopeak events as required for accurate quantification. The latter is given by the expression:

$$P(364) = C_{PP} - PS(364) - PS(637/723), \quad \text{Eq. 19}$$

where C_{PP} is the total count recorded within the photopeak window. Three scatter multipliers ($k_1 = PS(637/723)/US(637/723)$; $k_2 = LS(637/723)/US(637/723)$; and $k_3 = PS(364)/LS(364)$) will allow counts detected in the upper window (US) to be used to sequentially remove scatter events from the lower two windows (PP and LS). Once this is done, the 364-keV scattered photons that fall into the photopeak (PP) window can be removed. Techniques for estimating the scatter multipliers empirically by using the scintillation camera response to ^{137}Cs and ^{51}Cr (which when superimposed may be considered to simulate the ^{131}I spectrum) have been described (30).

iv. Digital Filtering Techniques. Scattered photon effects may also be removed through computer processing utilizing digital filter techniques. A number of methodologies have been implemented for both planar and SPECT imaging. The Wiener restoration filter has been shown to compensate for the blurring effects of scattering and collimator septal penetration (31–35). As a general rule, the Wiener filter uses minimization of the mean square error between the restored image and object function as the criterion for optimization. The technique exploits a priori estimates of the object and noise power spectrum determined from the degraded image.

Energy-weighted acquisition (EWA) represents a distinctly different image filtering approach in which a different spatial filter (weighting function) is applied for each energy to remove the effects of Compton scattering (36–39). The EWA approach uses all scintillation events and fractionally weights their contribution to the image formation, depending on energy. The sign and magnitude of the

weighting values are related to the probability that a given event represents scatter or primary radiation. For events more likely to be scattered photons, negative weights are assigned. The weighting function incorporates information about the instrument response (e.g., collimator characteristics and so on), as well as the scattering environment. Although, in principle, the weighting functions should be determined individually for each imaging configuration encountered in practice, functions specific to the given radionuclide and camera system may be stored and used successfully (36).

3. Single-View Effective Point Source Methods

Occasionally source volumes or features are seen on only one scintillation camera view. This may occur for a superficial source region with minimal uptake and/or relatively high background conditions. For these situations, a simplified single-view effective point source method (35,40) may be used instead of the conjugate view method. The activity calculation is based on the known (previously determined) effective linear attenuation coefficient, μ_e , and the measured depth of the source region, d , according to the expression:

$$A = I_A e^{\mu_e d} F / C, \quad \text{Eq. 20}$$

where I_A is the counts per unit time within the image ROI (denoted here as the anterior view), and C is the system calibration factor (count rate per unit activity). An orthogonal scaled image may be used to assist in depth determination. The factor F corrects for background activity that is counted within the ROI (see Eqs. 6 and 7).

B. SPECT Techniques

Because activity in under- or overlying regions and irregular distribution of background may interfere with accurate quantitation, SPECT imaging has the potential for improving the accuracy of planar imaging measurements. Quantitative SPECT (41-46) enables the determination of actual tissue activity concentration (e.g., MBq/cm³) and the associated total volume (e.g., cm³) over which the activity is distributed. Although attenuation correction schemes, nonoptimal statistics, collimator resolution and scatter result in some limitations to the accuracy of quantitative SPECT determinations of radioactivity, SPECT imaging can provide major advantages over planar conjugate pair imaging for selectively detecting and discriminating activity in source tissues from surrounding structures. The use of SPECT is particularly advantageous for measuring activity in regions in which activity in contiguous overlying, underlying or adjacent structures limit the accuracy of the conjugate pair planar view measurements. The use of appropriate SPECT acquisition parameters, a suitable reconstruction algorithm for image reconstruction and image processing, a properly calibrated imaging system and a constant distribution of radiopharmaceutical during the imaging procedure can all provide an accurate assay of radioactivity in vivo (41-46).

To date, the majority of reports have involved the use of a single rotating scintillation camera for SPECT image acquisition to determine activity in regions and tissues. The relatively low sensitivity of these systems has held back development of correction techniques that would allow improved accuracy for quantitating nonuniform activity distributions in inhomogeneous and irregularly shaped attenuation media (41-43,46-50). Numerous approaches have been implemented to correct for the limited counting statistics available from conventional SPECT imaging. Multiple detector SPECT systems, either multicamera or ring systems, and utilization of fanbeam and conebeam

collimators have each contributed to the improvement of the counting statistics available for SPECT. The use of filter functions with cutoff frequencies matched to the system's spatial resolution has proven to be useful for reducing the effects of statistical uncertainty (51-53).

Despite the limitations, SPECT has been used to measure activity levels in source tissues with acceptable accuracy and precision. The SPECT system must be properly calibrated to ensure acceptable reconstructed uniformity, sensitivity, spatial resolution, linearity and count rate performance. Acquisition variables must be selected to provide adequate counts per view, appropriate spatial and angular sampling and the desirable imaging orbit. Selection takes into consideration the intrinsic and system performance properties, in vivo activity levels at the time of measurement and the determination of imaging times based on subject comfort as well as the uptake and clearance properties of the radiopharmaceutical. In addition, suitable software for image reconstruction and image processing is necessary (41-45). Research into new methods for improving SPECT quantitation is under way, and the approaches for activity quantitation in vivo are expected to change as new methods are validated for scatter and attenuation correction.

Quantitative SPECT scans can be used for all imaging time points if the tomograph has sufficient sensitivity to keep acquisition time to reasonable intervals so that patients will tolerate the procedure. Alternatively, the sequential images can be acquired by planar procedures, with a SPECT image taken at one time point during the study. The result from the SPECT scan can be used to constrain the planar data at that point. Then, assuming that the image contrast is time invariant, one can apply the correction factor required for that constraint to the earlier and later planar-imaging results (54).

1. Phantom Studies

The use of software-generated phantoms and fabricated anthropomorphic phantoms is recommended to test and validate the performance properties of the SPECT system as well as the reconstruction and correction methods, and to develop calibration factors for converting counts observed in ROIs to activity levels (42,43). Phantoms that replicate the size, shape, electron density, mass density and elemental composition of the source tissues and surrounding structures can be used with activity levels comparable to the range expected in human subjects to obtain these calibration factors for SPECT image quantitation.

2. Reconstruction Methods and Attenuation

SPECT reconstruction and image restoration may be implemented using either an iterative or noniterative algorithm (41). A critical parameter affecting the accuracy of SPECT data is attenuation. Attenuation compensation is performed either by assuming uniform attenuation throughout the body, or measurement of the nonuniform attenuation coefficient distribution. Compensation methods for the uniform attenuation assumption used in SPECT can be divided into three classes: preprocessing correction, intrinsic correction and postprocessing correction. The most widely used approach in current commercial SPECT systems is Chang's first-order postprocessing method (55), wherein the image is initially reconstructed using filtered backprojection and then multiplied on a voxel-by-voxel basis by a mean depth-dependent attenuation correction. The applicable equation is:

$$CF = \frac{1}{\frac{1}{N} \sum_{i=1}^N \mathcal{T}_i}, \quad \text{Eq. 21}$$

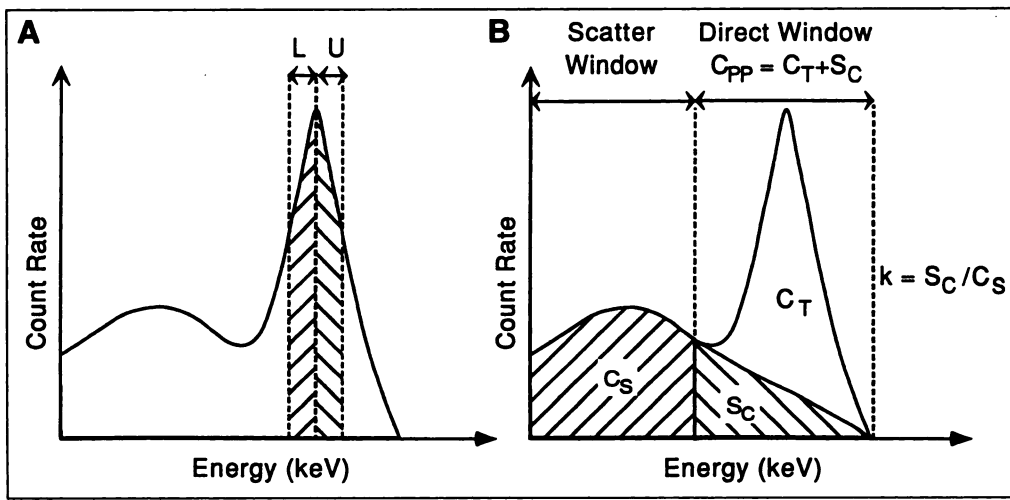


FIGURE 5. Dual-energy window techniques. (a) The photopeak is divided into two equal nonoverlapping windows (lower, L; upper, U) which encompass the standard symmetric acquisition window. Adapted from a previous report (28). (b) The spectrum is divided into a scatter window where the counts are attributed entirely to lower-energy scattered photons (C_S) and a direct window over the photopeak where the observed counts (C_{PP}) are composed of both scattered (S_C) and true photopeak (C_T) counts. The assumption is made that the scattered counts S_C are correlated with C_S by the same constant k for all image pixels. Adapted from a previous report (26).

where CF is the correction factor, \mathcal{T}_i is the transmission at angle i from the voxel through the body to the skin surface and N is the total number of projections. This correction is quantitatively rigorous only for uniformly attenuating media. Such uniform attenuation is often assumed for abdominal imaging. With commercial systems, the skin surface is either defined by the user or by a simple algorithm. A typical algorithm uses an intensity threshold that is a prechosen percentage of the maximum intensity in the image. This image can either be a single transverse slice, a sum of several slices, or a composite of all the slices in the reconstruction.

In areas of nonuniform density, such as the thorax, a nonuniform attenuation map should be used. This map can be calculated from radioisotope transmission data obtained at the same time the emission data is being acquired. The source of the radiation can be a sheet source (56), a translating line source with parallel-hole collimation (57), a point source with cone-beam collimation (58) or a line source with fan-beam collimation (59–61). Some multihead commercial systems currently provide such an option (62,63). An important parameter in these procedures is the collimation used. For example, fan-beam collimation can lead to truncation of the data at the edge of the patient. A compensation for this truncation must then be used. The relative merits of different methods of collimation are still under investigation.

Another option in the case of nonuniform attenuation is the use of an attenuation map obtained from a CT image by a suitable energy extrapolation from the gamma-ray energy of the x-ray scanner (~ 70 keV) to the energy of the gamma ray of interest (54,64). This map is useful only if the CT image set can be fused (i.e., superimposed exactly) into the space of the SPECT image set. Various methods have been proposed for image fusion (65–67).

The nonuniform attenuation map can be incorporated into the Chang attenuation compensation method (50,68,69) or applied through an intrinsic attenuation correction. The latter usually occurs by means of one of many iterative reconstruction algorithms. These algorithms rely on finding a consistency between the measured data and results from the current estimate of the image after forward projection to the detector. The forward projection utilizes a model to specify the process. Within that model, the attenuation is usually accomplished one voxel at a time by the formula

$$I' = I_0 e^{-\mu l}, \quad \text{Eq. 22}$$

where I_0 is the gamma-ray intensity entering the voxel, I' is the intensity (count rate) leaving the voxel, μ is the average

attenuation coefficient within the voxel and l is the gamma-ray path length through the voxel at the projection angle of interest. Examples of reconstruction algorithms available are the maximum-likelihood expectation-maximization (ML-EM) algorithm (69) and the space-alternating generalized EM (SAGE) algorithm (70). The utility of nonuniform attenuation correction with an iterative algorithm has been verified by tests of relative diagnostic accuracy in coronary heart disease (71).

3. Scattered Photon Correction Methods

Several different approaches have been advocated to reduce the detrimental effects of detected scattered photons on activity quantitation and on image quality (28,41–43,72–83). These methods include use of a reduced-value attenuation coefficient, dual- or multiple-energy window acquisition, convolution/deconvolution methods (in space or energy), spectral fitting, energy-weighted acquisition and computer modeling. Most of these methods are applicable to planar imaging as well.

The reduced-value attenuation coefficient approach (broad-beam geometry) compensates for the additional scatter counts present by undercorrecting the measured image counts. Dual-photopeak window methods provide a subtractive method for correction of scattered photons within the lower energy portion of the photopeak (28,78–81). In one technique, the photopeak region is divided into two nonoverlapping energy windows (Fig. 5a) from which a regression relationship is obtained between the ratio of counts within these windows and the scatter contribution within the total photopeak window (28). The scatter distribution within the photopeak window is estimated through calibration to determine the regression coefficients for the specific system and pair of energy windows without the use of arbitrary scaling factors. The more generalized scheme for dual-window acquisition involves acquiring two sets of images, one at the radionuclide photopeak and a second one suitably positioned to image Compton scattered photons. An appropriate fraction of the scatter image is subtracted from the photopeak image to compensate for the Compton scatter photons (80,81).

Koral et al. (80) have described a method which utilizes an adjacent lower energy scatter window to obtain a scatter multiplier “ k ” defined as the ratio of the scattered counts in the photopeak window to those in the lower window (Fig. 5b). The true photopeak counts C_T are given by the simple relationship:

$$C_T = C_{PP} - kC_S, \quad \text{Eq. 23}$$

where C_{PP} is the total count recorded within the photopeak window and C_S is the count within the scatter window. The

multiplier k may be determined empirically from imaging experiments conducted with sources inside scattering medium phantoms and in air.

Deconvolution techniques are either true deconvolution methods (83–85) or convolution calculations that produce a scatter estimate which is subtracted from the usual image to provide correction (74). A scatter function (74,84,85) or an energy-response function (83) is required to carry out the calculation. The scatter function has spatial “tails” that define the magnitude and extent of the effect of detecting scattered photons. It is usually measured by placing a radioactive source within a water bath that provides the representative scatter. The energy-response function simulates the detection process of the scintillation camera; a Gaussian shape with a width depending on energy is usually assumed.

In some spatial convolutions, the calculation begins with a first approximation to the corrected image (74,86). This estimate would ideally be improved upon through an iterative process. However, only one iteration is actually performed to avoid noise increments and potential instabilities.

Energy-weighted acquisition is a technique available through an add-on to a commercial gamma camera system (87,88). It requires the knowledge of predefined weights, which are derived from desired criteria for the resulting images. These criteria are improved resolution without increase in noise and stability against changes in energy gain from point to point over the camera face (39). Spectral-fitting methods (82) are also now available on a commercial system (89). Last, computer modeling (90) is an elegant technique but potentially requires an accurate Monte Carlo simulation of photon transport for the particular patient of interest (91).

Simulation studies in heart perfusion, especially in cases of large liver activity, have led to the conclusion that both attenuation and scatter correction are needed (92,93). However, because of the complexity of the problem and due to the multiplicity of proposed methods, no one single method of scatter correction has been widely accepted, although scattered photons may account for as much as 50% of the recorded counts in a SPECT image.

4. Activity Determination

Reasonably accurate and precise quantitative SPECT imaging is clinically feasible, even without sophisticated scatter corrections, at least in uniformly attenuating parts of the body such as the abdomen and pelvis (42). With Chang's first order postprocessing method of attenuation compensation (55), the most commonly used approach in commercial SPECT systems, investigators have obtained fairly accurate activity estimates using a semi-automated processing method employing thresholding (94,95). The attenuation-corrected reconstructed slices are used to obtain source region activity based on a fixed threshold method. Briefly, all the reconstructed slices spanning the object of interest typically are analyzed to determine the maximum voxel count. Only voxels containing more than a predetermined percentage of this maximum count, as derived from phantom studies, are included for the activity calculation. The activity is determined from the sum of the counts in the included voxels divided by the acquisition time and an independently acquired count rate per unit activity system calibration factor. In addition to threshold methods (96,97), image segmentation has also been based on edge detection (98–101).

It should be pointed out that any technique that does not specifically compensate for scatter will not be rigorously correct, especially in the presence of low-energy photons, which are known to contribute a significant amount of scatter.

In areas of nonuniform density, such as the thorax, it is necessary to incorporate a nonuniform attenuation map in the Chang attenuation compensation method (102). Also, the use of a fixed threshold method to distinguish between source and background voxels is based on a global maximum and can be incorrect if the activity in the selected volume of interest changes rapidly with time. In addition, Mortelmans et al. (103) reported that a single fixed threshold value may not be accurate enough because the threshold value was found to be dependent upon object size and image contrast.

Because SPECT is a three-dimensional imaging modality, it can provide information about the distribution of activity within a source volume (i.e., the activity in each individual voxel may be obtained). However, in practice, this may be difficult due to the large uncertainty associated with quantitating radioactivity within a very small volume (i.e., the voxel) due to finite system spatial resolution and partial volume effects (42,99). To minimize this problem, the average activity within a collection of subvolumes, each containing an appropriate number of voxels, may have to be integrated (104). A number of investigators have determined the spatial distribution of activity within a source region at the voxel level (104–108) and used these data to generate patient-specific absorbed dose estimates. In addition, image fusion (i.e., registration of multimodality images), has also been shown to be important for patient-specific dosimetry in radionuclide therapy (104,105,107,108). Bolch et al. (4), in the last issue of *The Journal of Nuclear Medicine*, provide a more comprehensive treatment of nonuniform activity and absorbed dose distributions.

C. PET Techniques

Quantitative PET imaging is generally thought to be more accurate than SPECT, largely because of the commercial availability of a convenient attenuation correction (109). Standard PET corrections are made for detector nonuniformity, deadtime, random coincidences and attenuation; otherwise, the procedure is similar to that for SPECT. PET is sometimes used for measuring activity of a positron emitter to simulate another radionuclide of the same atomic number (not a positron emitter), for which activity measurements and absorbed dose estimates are desired. The assumption is made that isotopes have the same biokinetic behavior. For example, measurements have been made using an ^{124}I -labeled radiopharmaceutical as a surrogate for the ^{131}I -labeled radiopharmaceutical (110). Unlike most positron emitters, ^{124}I has a sufficiently long half-life (4.2 days) to permit imaging over several days during the biologic uptake and washout of the agent. Therefore, when an analogous positron-emitting isotope (e.g., as a surrogate for a desirable therapeutic radionuclide) that has a physical half-life long enough relative to the pharmacokinetics is available, PET imaging may increase the accuracy of activity measurements.

V. QUANTITATIVE MEASUREMENT TECHNIQUES: NON-IMAGING

A. External Nonimaging Radiation Monitoring

Whole-body retention can be estimated by placing a shielded NaI detector or other suitable survey meter 3–7 m from the patient and recording the number of counts detected (111). A source of known activity is used to calibrate the detector. Initial measurements for the total body must be made within a short time after administration, defined as within the “no patient excretion” period, so that later measurements may be easily and more accurately compared to initial body content of the administered activity and to the reference standard. The use of a reference standard measured at each time corrects for radioac-

tive decay and for instrumental drifts. Special care must be taken to minimize errors from fluctuating background (such as might be caused by external radionuclide sources or other injected patients). These whole-body measurements are performed at each patient imaging session to obtain the biologic retention of activity in the total body. Whole-body counters with dual-opposed NaI(Tl) detectors have also been used to measure whole body radioactivity (112).

B. Tissue Sample Counting

The most frequently sampled tissue is blood (113). The temporal variation of activity in blood may be important for assessing bone marrow dose and providing input functions and central compartments for some compartmental models. If bone marrow dosimetry is desired, the hematocrit and the red marrow extracellular fluid fraction for the patient should also be obtained (114). Activity may be determined using a variety of instruments including dose calibrators, gamma well counters and liquid scintillation counters. A calibrated (through the use of appropriate standards) gamma well counter is commonly used to obtain serial blood activity concentration ($\mu\text{Ci/ml}$). Typically, 1–3 ml of blood are withdrawn by peripheral venipuncture from the patient at various times postadministration, such as 5 min, 10 min, 15 min, 30 min, 60 min, 120 min, 24 hr, 48 hr and 72 hr. Samples may need to be taken at later times postinjection, depending on the half-life of the radionuclide and the blood retention rate.

Another approach for blood pool analysis is the use of time–activity data generated from conjugate view quantitative images of the chest. Regions of interest can be drawn around either the left ventricle of the heart or the aorta. The activity data determined from the quantitative conjugate view images has been validated in the literature by comparison to the serial blood activity data in the same patient (115). However, this technique may not be accurate when there is radionuclide uptake in the myocardium.

Finally, an estimate of the activity retained in tissues and regions may be obtained through serial biopsy sampling of the tissue of interest (116). Most frequently, this is not a viable option. However, in therapeutic radionuclide protocols, biopsy samples or tissue samples might be obtained after surgical resection from one or more tissues of interest, such as tumor, liver, lymph node and so on. Also, a tissue may be biopsied for other clinical reasons and a sample obtained (or portion thereof) for quantitation in a calibrated well counter. The biopsy sample may be useful in deriving an empirical conversion factor (count rate/activity) for scintigraphic images of the same tissue in vivo.

C. Excreta Counting

Characterization of the total amount (or fraction) of activity excreted, excretory rates and routes of excretion are essential for estimating absorbed doses (113). However, direct measurement of excretion rates per se is rarely performed. Total-body retention as determined from imaging or radiation monitoring may be used to assess excreted activity. The four major routes of excretion are urine, feces, perspiration and exhalation. Of the excretory pathways, the fraction of the administered activity excreted in the urine is most easily determined. Urine collection is the method of choice. The urine sampling must be complete in the sense that all voidings should be collected or pooled over a specified period (e.g., 0–6 hr, 6–12 hr, 12–24 hr and so on) and labeled as to time of collection. This measurement is important for two reasons. First, the total amount excreted and the rate at which it is excreted are a major determinant of the total-body retention and dose to bladder. The activity in the urine after voiding should not be included in the total body or

remainder of the body activity retention. Second, from the total-body retention, one can then calculate the residence time (or cumulated activity) for the urinary bladder contents using the model of Cloutier et al. (117). Dose to the urinary bladder wall surface may be calculated using the dynamic bladder model of Thomas et al. (118).

The storage and accurate measurement of highly radioactive urine can be a radiation safety problem. Also, protocols which rely on patient self-measurement of void volume before urine aliquots are prepared may yield unreliable results depending on the continence of the patient. Therefore, whole-body monitoring to determine whole-body retention for calculation of bladder wall dose is preferable to making urine measurements when the major excretory route is via urine.

Fecal excretion is determined for fewer compounds than is urinary excretion. Stool radioassay is infrequently done and may be estimated as the difference between total-body retention and urinary excretion (assuming negligible elimination by exhalation and perspiration and complete urine collection). Activity can accumulate in the gastrointestinal (GI) tract from three sources: orally administered compounds that are not absorbed or are incompletely absorbed; hepatic filtration with subsequent biliary excretion to the small intestine; or secretion into stomach and into the GI tract lumen. All luminal activity that is not absorbed is excreted in the feces. One may use the ICRP-30 GI tract model (119) under conditions of continuous flow of material to calculate residence times for the organs comprised by the GI tract. Other models are available which explicitly consider bolus transport through the GI tract (120).

Significant excretion by the remaining two routes, perspiration and exhalation, are rare and perhaps the most difficult to measure accurately. However, in specific instances, they may be important. For example, the amount of ^{14}C -labeled carbon dioxide exhaled is critical for estimating the absorbed dose associated with the ^{14}C urea breath test. In this test, 40–90% of the administered activity is excreted in the breath or urine within a few hours (121). The remaining activity is incorporated into bone with a long biologic half-time. The bone dose will vary substantially depending on how much ^{14}C -labeled carbon dioxide is excreted; therefore, an accurate assessment of the fraction exhaled is critical. The total fraction of a radionuclide excreted by perspiration is difficult to assess. Iodine is known to utilize this mode of excretion.

VI. DATA PROCESSING

A. Curve Fitting and Determination of \bar{A} and τ

The activity (number of nuclear transitions per unit time) in region h is a function of time t and is symbolized as $A_h(t)$. From serial activity measurements (obtained from external counting, tissue sampling or excreta sampling), one can determine the area under the time–activity curve, \bar{A} (2). The cumulated activity, \bar{A}_h , is the sum of all nuclear transitions in region h during the time interval of interest. The residence time, τ_h , is obtained by dividing \bar{A}_h by the administered activity, A_0 .

Several methods are available for determining \bar{A}_h from graphical representations of $A_h(t)$. Among these are numerical methods such as the trapezoidal rule (122) and Simpson's rule (123), and analytical methods (124), based on the assumption that some fitting function can adequately describe the data. In particular, if $A_h(t)$ can be fitted to a sum of exponentials, the function can be written as:

$$A_h(t) = \sum_j A_j(0)e^{-(\lambda + \lambda_j)t}, \quad \text{Eq. 24}$$

where $A_j(0)$ is the initial activity value of the j th exponential component, λ is the physical decay constant corresponding to the physical half-life T of the radionuclide through the relationship $\lambda = 0.693/T$ and λ_j is the biologic elimination constant corresponding to the biologic half-time T_j ($\lambda_j = 0.693/T_j$) of the j th exponential component. Summing all the nuclear transitions during the time interval is equivalent to integrating $A_h(t)$ over that time interval. The limits of the integral are usually taken as time zero to infinity:

$$\tilde{A}_h = \int_0^{\infty} A_h(t) dt = \sum_j A_j / (\lambda + \lambda_j) = 1.443 \sum_j A_j (T_j)_e, \quad \text{Eq. 25}$$

where $(T_j)_e = 0.693 / (\lambda + \lambda_j)$. $(T_j)_e$ is the effective half-time of the j th exponential component, where the combination of physical decay and biologic removal results in an exponential disappearance rate that is the sum of the physical and biologic decay rates. The quantity A_j is negative for uptake components.

Analytically, the A_j and λ_j values can be determined by fitting the $A_h(t)$ data to Equation 24 by a least squares technique (see Example 4 in Appendix E). In some cases, adequate results can be obtained by plotting $A_h(t)$ on semilogarithmic graph paper, drawing the best-fit line through the data corresponding to the slowest component (which will be a straight line), subtracting its values from the original data, and repeating the process to generate the A_j and λ_j values.

Alternatively, \tilde{A}_h may be calculated as the area under the curve in an ordinary plot of $A_h(t)$, by use of any of several numerical methods, such as Simpson's rule or the trapezoidal rule. Of these, the simplest to apply is the trapezoidal rule (122):

$$\int_a^b A_h(t) dt = [w_1 y_0 + (w_1 + w_2) y_1 + (w_2 + w_3) y_2 + \dots + w_m y_m] / 2, \quad \text{Eq. 26}$$

where w 's are the widths and y 's are the heights of the m rectangles. An example of the use of the trapezoidal rule can be found in Example 4 of Appendix E.

These curve processing methods can be applied to any source region time-activity data. The resulting cumulated activities or residence times can then be used to estimate absorbed radiation dose using the MIRD schema (1,2). However, obtaining the residence times for the remainder of body, excretory organs and regions that cannot be measured directly is often difficult. Data sets for whole body and cumulative or differential excretion and other regions may require interpretation and manipulation.

B. Compartmental Modeling

An alternative approach to the direct calculation of \tilde{A} and τ is to fit a compartmental model to the measured data. Often, it is impractical to measure the time-activity curves of all of the source regions. When the physiological interactions of these regions with the blood or with other directly measurable tissues are known, the time-activity curves of unmeasured tissues can be inferred by compartmental modeling. This technique also makes it feasible to separate the time-activity curves of overlapping regions from each other. A compartment in such a model is a unit of the body which is assumed to act kinetically as a distinct, homogeneous, well-mixed unit (125). For example, if a kidney agent is studied, the renal cortex and renal medulla might be treated as separate measurable compartments, whereas the liver would probably be a single compartment. On the other hand, if the agent studied is a hepatic agent, the liver

would probably be divided into several compartments, including a gallbladder compartment that receives activity from one or more of the intrahepatic compartments. The gut, which subdivides anatomically into a number of compartments, would also be important in a liver agent model because it receives activity from both the liver and gallbladder. But the gut may also receive activity directly from the blood through the mesenteric circulation. If the tracer is partially or completely reabsorbed, the gut sends activity back to the liver and, perhaps, to the blood. In the study of a liver tracer, the kidney would probably be treated as a single compartment.

A compartmental model, for dosimetry purposes, describes the kinetics of the tracer in question as transfers among the compartments of interest. These compartments may represent individual organs, in which case the normal assumptions about a compartment, e.g., being a well-mixed space, are not strictly valid. Usually, however, a reasonable representation of the organ's kinetics may be obtained through the analysis and an accurate residence time may be determined. Alternatively, compartments may represent pools or spaces in the body, and the residence time obtained must later be apportioned to individual regions to estimate the radiation dose. In dosimetry studies, as many as possible of these compartments are measured directly. All available data are used and known physiology furnishes the configuration of the model. Some of the parameters of the model may be taken from the literature, especially when observed data are not sufficient to identify the model completely. The more compartments for which valid data exist to test the model, the more confidence one can place on the model projections of the time-activity functions for those compartments without direct observational data.

Most models assume linear (first-order) kinetics between linked compartments. In other words, transfer out of a compartment per unit of time is a constant fraction of the content of that compartment. Therefore, the time-dependent activity of any compartment can be described by a differential equation, and the entire system is described by a series of coupled differential equations. Even when a transfer of tracee is nonlinear, the use of tracers linearizes the function. When the steady state is perturbed during a study (e.g., a large dose of iodine is given during a radioiodine study or cholecystokinin is given during a gallbladder study), this perturbation may be modeled by adjusting one or more of the model parameters. Radioactive decay is incorporated into the physiological model as an exit rate constant from each compartment.

Compartmental models are described by a set of differential equations, the parameters of which are the sizes of the compartments and the rate coefficients for transfer between compartments. Unless the model is quite simple (four compartments or less), the only practical way to solve these models is by numerical methods. Analytic solutions for small models which have unique solution sets are known, and software is available for generating the rate constants from the input data points (126,127). Because the transfer rate coefficients in these models are assumed to be linear (i.e., they do not vary with time), extrapolation of the results beyond the end of the measured data to infinite time, using these coefficients, is often thought to be a reasonable approach, assuming the model accurately represents reality (which may not be the case for short-term bone models, for example; see Appendix D). A variety of programs are available for solving models and can be used on desktop computers (128). The most useful programs have utilities for optimizing the fit of time-activity curves of the model solution to the observed data through the use of iterative, nonlinear least squares routines.

Once the best model to describe a tracer system has been determined and fitted to the available data, time-activity functions for all of the regions and tissues of importance to dosimetry are generated and projected to infinite time using the parameters determined by fitting all of the available data sets (129). These functions are then integrated to obtain \tilde{A} and τ .

VII. SUMMARY

For those who are involved in the design and execution of experimental trials with radiopharmaceuticals, whether the desired endpoints are preclinical efficacy, diagnostic utility, clinical therapeutic applications or acquisition of dosimetry data for correlation with biological response, methods for data collection, analysis and processing must be carefully constructed in advance (a study design protocol checklist is provided in Appendix B). Not only does this hold true for arriving at the most accurate method to assess product utility, but frequently such careful forethought can achieve labor and cost savings in the laboratory or clinic.

Calculational methods described in this article have used the MIRD schema for absorbed dose assessment. Analytical methods for prospective design of experimental trials have been addressed through consideration of information already known about the radiopharmaceutical for estimating the appropriate number of experimental sampling points to be obtained based on uptake and retention properties. An accurate determination of the time-dependent activity in situ is required for calculating absorbed dose to target regions. The determination of cumulated activity \tilde{A} and residence time τ involves establishing a prospective plan for data collection, analysis and processing. After identifying all source regions with adequate temporal sampling, the absolute activity in each of these regions versus time must be determined. Quantitative measurement techniques such as conjugate view planar imaging (as well as SPECT and PET imaging), external nonimaging radiation monitoring, tissue sampling (blood or biopsy) and excreta sampling have been presented in detail with emphasis on data analysis. Diagrams (Figs. 1-5), examples in the appendices and the extensive references cited are intended to provide the reader with the basic "tools" for collecting and analyzing experimental radiopharmaceutical data sets.

Last, in the data processing phase, integration of time-activity curves provides the cumulated activity and thus residence time in each source region from which region and total body absorbed dose can be calculated. Several "how-to" examples (Appendix E), including trapezoidal rule, Simpson's rule and analytical methods using least squares procedures have been included to provide calculational details. Compartmental modeling techniques have been described also. Nonuniform uptake and retention at the suborgan level (or smaller) is the subject of a separate MIRD publication (4) and is not considered in any detail here.

The aim of this pamphlet on methods for the collection and analysis of radiopharmaceutical biodistribution data is to provide the investigator with referenced, standardized and accepted methodology for the accurate determination of absorbed dose from internal emitters. The document is intended also to serve as a guide for choosing the appropriate techniques when acquiring and preparing product data for review by national regulatory agencies.

ACKNOWLEDGMENT

We gratefully acknowledge the assistance of Ranasinghage C. Samarasinghe, PhD, in preparing the figure artwork.

APPENDIX A: SYMBOLS AND DEFINITIONS

See Table A1.

APPENDIX B: STUDY DESIGN AND PROTOCOL CHECKLIST

Dosimetry Evaluation

Radionuclide: _____ Compound: _____

Date: _____ Performed By: _____

A. Data Collection Methods

Direct sampling performed? (Y/N)

Blood _____ Tissues _____ Excreta _____

Imaging Type: Planar _____ SPECT _____ PET _____

Other _____

Corrections: Decay _____ Attenuation (Method) _____

Scatter (Method) _____ Image Filter _____

Data Source: Literature _____ Animal (specify) _____

Human _____ Other _____

Number and Times of Serial Measurements:

Blood/Plasma _____ Imaging _____

Tissue _____ Excreta _____

Were initial data obtained pre-void? (Y/N)

Other comments on data collection techniques:

B. Data Analysis

Methods of Absolute Activity Determination

C. Data Processing

Determination of \tilde{A} or τ

Type of Mathematical Model: 1. Numerical Integration _____

2. Least Squares _____ 3. Compartmental

Model _____ 4. Other _____

If (1) or (2), what assumptions were made about the activity beyond the end of the data set?

How was red marrow \tilde{A} or τ determined? _____

Does model account for excretion? (Y/N) _____

Does model account for 100% of the activity? (Y/N) _____

D. Dosimetry Methods

Dosimetry Schema: MIRD _____ ICRP _____ Other _____

Source of S values _____

Method of Calculation (e.g., by hand or computer program - specify version) _____

Other Models Used (check all that apply)

ICRP Lung Model _____ ICRP GI Model _____

Dynamic Bladder Model _____ Other _____

Corrections Applied: Remainder of body S values _____

Adjustments for patient body size, region size/mass

Describe any other assumptions:

E. Checklist Review

Signed: _____ Date: _____

TABLE A1
Table of Symbols and Definitions

Section	Symbol	Definition (units)
II	$\bar{D} = \bar{A} \times S$	Mean absorbed dose (Gy or rad)
	\bar{A}	Cumulated activity (Bq · sec or $\mu\text{Ci} \cdot \text{hr}$)
	S	Mean absorbed dose per unit cumulated activity: S value (Gy/Bq · sec or rad/ $\mu\text{Ci} \cdot \text{hr}$).
	$\tau = \bar{A}/A_0$	Residence time (sec or hr).
III.C.	A_0	Administered activity (Bq or μCi).
	T	Physical half-life (sec or hr).
	T_e	Effective half-time (sec or hr).
	t = 0	The time of radiopharmaceutical administration.
IV.A.2.	A/P	Anterior and posterior.
IV.A.2.a.i.	t_j	Thickness of a single source in region j (cm).
	t_n	Thickness of region n (cm).
	μ_j	Linear attenuation coefficient of source region j (cm^{-1}).
	μ_n	Linear attenuation coefficient of region n (cm^{-1}).
	t	Patient thickness (cm).
	I_{AP}	Conjugate view count rate pair (anterior/posterior) (counts/time) (s^{-1} or min^{-1}).
Eq. 1	$A_j = \sqrt{\frac{I_{AP} f_j}{e^{-\mu_j t}}}$	Source activity in region j (Bq or μCi).
Eq. 2	$f_j = \frac{(\mu_j t/2)}{\sinh(\mu_j t/2)}$	Correction factor for the source region attenuation (μ_j) and source thickness (t) (i.e., source self-attenuation correction).
Eq. 3	$\mu_e = (1/t) \sum_{i=1}^n \mu_i t_i = \mu_j + (1/t) \sum_{i=1}^n (\mu_i - \mu_j) t_i$	Effective linear attenuation coefficient (cm^{-1}).
IV.A.2.a.i.	$e^{-\mu_e t}$	Transmission factor (\mathcal{T}) across the patient thickness t.
	t	Patient thickness through the region of interest (cm).
	μ_e	Effective linear attenuation coefficient across the patient thickness (cm^{-1}).
	I/I_0	Ratio of count rates with (I) and without (I_0) the patient in position.
	C	System calibration factor (count rate per unit activity) ($\text{Bq}^{-1} \text{sec}^{-1}$ or $\mu\text{Ci}^{-1} \cdot \text{min}^{-1}$).
IV.A.2.a.ii.		
Eq. 4	$A_2 = \sqrt{\frac{I_{AP} f_2}{e^{-\mu_e t}} g(\alpha)}$	Activity in source volume 2 (Bq or μCi).
Eq. 5	$g(\alpha) = \{1 + (\alpha f_2/f_1)^2 + 2\alpha(f_2/f_1) \cosh[(\mu_2 t_2 + 2\mu_3 t_3 + \mu_4 t_4/2)]^{-1/2}$ $\alpha \equiv A_2/A_1$	Correction factor for two separate overlapping source regions of uniform activity.
IV.A.2.b.i.	$(I_{AP})^{1/2}$	Ratio of the activity in the two overlapping source regions.
Eq. 6	$F = \{[1 - (I_{ADJ}/I_A)(1 - t_j/t)][1 - (I_{ADJ}/I_P)(1 - t_j/t)]\}^{1/2}$	Geometric mean of the A/P count rate pair (counts/time).
	I_{ADJ}	Fraction of the geometric mean count rate that originates from the organ (or volume) of interest alone. Correction factor for surrounding background activity.
Eq. 7	$F \equiv [1 - (I_{ADJ}/I_A)(1 - t_j/t)]$	Count rate from a region adjacent to the source region-of-interest (ROI) (sec^{-1} or min^{-1}).
IV.A.2.b.ii.		Simplified expression for the correction factor F (Eq. 6) for the situation in which the source is located near the midline.
Eq. 8	$A_3 = \sqrt{\frac{I_{AP} f_3}{e^{-\mu_e t}} k(\gamma)}$	Activity in uniform source region 3 surrounded by uniform background activity (Bq or μCi).
Eq. 9	$k(\gamma)$	Correction factor for surrounding uniform background activity in regions 2 and 4.
	$\gamma_2 \equiv A_2/A_3$	Ratio of the activity in the background regions of 2 or 4 to the activity in source region 3.
	$\gamma_4 \equiv A_4/A_3$	
IV.A.2.c.i.	\mathcal{T}	Relative transmission as a function of depth within a scattering medium.
	$\mathcal{T} = I/I_0 = e^{-\mu_e t}$	Transmission modeled as a single exponential (straight line on a semi-log plot).
	μ_e	Effective linear attenuation coefficient (cm^{-1}).
	$\mathcal{T} = ne^{-\mu_e t}$	Expression for transmission in the straight line region (semi-log plot) beyond the characteristic shoulder.
	μ_0	Equivalent narrow-beam geometry linear attenuation coefficient (cm^{-1}).
	n	Pseudo-extrapolation number.
Eq. 10	$A_j = \sqrt{\frac{I_{AP} f_j}{n \mathcal{T}} C}$	Source activity for single source embedded within a scattering medium with no surrounding background activity. Valid for source regions located at depths beyond the transmission curve shoulder.

TABLE A1
Continued

Section	Symbol	Definition (units)
IV.A.2.c.ii.	DDBF	Acronym for depth-dependent buildup factor in Eqs. 11 and 12 for I_A and I_P .
Eq. 13	$B(d) = \frac{C_d}{C_{0,d}e^{\mu d}}$	Depth-dependent buildup factor.
	d	Depth at the center of the source (lesion) (cm).
	C_d	Count rate measured at depth d (sec^{-1} or min^{-1}).
	$C_{0,d}$	Count rate measured in air at same source to gamma camera distance (sec^{-1} or min^{-1}).
	μ	Linear attenuation coefficient (cm^{-1}).
	t	Overall patient thickness (cm).
	t_j	Source thickness (cm).
	$A_j = C_{0,d}/C$	Activity (buildup factor method) (Bq or μCi).
	C	System calibration factor (count rate per unit activity) ($\text{Bq}^{-1} \cdot \text{sec}^{-1}$ or $\mu\text{Ci}^{-1} \cdot \text{min}^{-1}$).
Eq. 14	DIBF	Acronym for depth-independent buildup factor.
	$\mathcal{T} = 1 - (1 - e^{-\mu d})B^{(\infty)}$	Transmission (DIBF method).
	$B^{(\infty)}$	Buildup factor at infinite depth. (Equivalent to the pseudo-extrapolation number, n).
IV.A.2.c.iii.	CR	Acronym for the channel ratio method.
	TEW	Acronym for the triple energy window technique.
Eq. 18	$C_T = C_{PP} - C_{LS} - C_{US}$	Corrected (true) photopeak counts.
	C_{PP}	Total count recorded within the photopeak window.
	C_{LS}, C_{US}	Counts within lower and upper scatter windows.
	k1, k2, k3	Scatter multipliers.
IV.A.2.c.iv.	EWA	Acronym for energy weighted acquisition.
IV.A.3.		
Eq. 20	$A = I_A e^{\mu d} F/C$	Activity seen only on one view (versus the conjugate method).
	I_A	Count rate within the image ROI.
	C	System calibration factor (count rate per unit activity).
	F	Correction factor for background activity counted within the ROI.
IV.B.2.		
Eq. 21	$CF = \frac{1}{\frac{1}{N} \sum_{i=1}^N \mathcal{T}_i}$	Correction factor (SPECT imaging).
	\mathcal{T}_i	Transmission at angle i from the pixel through the body to the skin surface.
	N	Total number of projections.
Eq. 22	$I' = I'_0 e^{-\mu \ell}$	Gamma ray intensity leaving a voxel.
	I'_0	Gamma ray intensity entering the voxel.
	μ	Average linear attenuation coefficient within the voxel (cm^{-1}).
	ℓ	Gamma ray path length through the voxel at the projection angle of interest.
IV.B.3.	k	Scatter multiplier defined as the ratio of the scattered counts in the photopeak window to those in the lower window.
Eq. 23	$C_T = C_{PP} - kC_S$	True photopeak counts.
	C_{PP}	Total count recorded within the photopeak window.
	C_S	Count within the scatter window.
V.B.	$\mu\text{Ci/ml}$	Units for blood activity concentration.
VI.A.	$A_h(t)$	Activity in organ h is a function of time t.
	t	Time.
Eq. 24	$A_h(t) = \sum_j A_j(0)e^{-(\lambda + \lambda_j)t}$	
	$A_j(0)$	Initial activity value of the jth exponential component.
	λ	Physical decay constant.
	λ_j	Biologic disappearance constant.
Eq. 25	\bar{A}_h	Cumulated activity in organ h during time interval of interest. (Area under the activity-time curve) (Bq s or Ci h).
Eq. 26	$(T_j)_e$	Effective half-time of jth exponential component (s or h).
	m	Number of rectangles (using trapezoidal rule).
	w	Width of rectangles.
	y	Height of rectangles.

TABLE A1
Continued

Section	Symbol	Definition (units)
Appendix C.1.1		Count rate with transmission source viewed through the patient.
	I_0	Count rate with the transmission source in air.
	I_{pt}	Count rate obtained with patient alone (counts/time).
Eq. C1	$A = F \sqrt{\frac{I_A I_P}{\mathcal{T}}} \frac{f}{C}$	Absolute activity A (MBq or μ Ci) in each region.
	F	Background correction factor (Eq. 6).
	f	Correction for source region attenuation and source thickness (Eq. 2).
Appendix D.1. A_1, A_2		Component coefficient for source region at t = 0 (fractional activity, unitless).
	T_e	Effective half-time (sec or hr).
	T_h	Residence time in source region h (sec or hr).
	$A_{inst}(t)$	Activity associated with instantaneous uptake.
	T_{inst}	Residence time assuming instantaneous uptake (sec or hr).
	k	Fractional error in residence time calculations.
	t_{max}	Time at which time-activity equation reaches a maximum.
	$T_{e1} = 0.693/(\lambda + \lambda_1)$	Effective half-time for uptake or rapid washout.
	$T_{e2} = 0.693/(\lambda + \lambda_2)$	Effective half-time for single component removal or slow washout.
Appendix D.2. $A_{long}(t)$		Activity associated with the effective half-time of the slow washout, T_{e2} .
	T_{long}	Residence time associated with $A_{long}(t)$.
Appendix D.3. $A_{rapid}(t)$		Activity associated with the effective half-time of the rapid washout, T_{e1} .
	T_{rapid}	Residence time associated with $A_{rapid}(t)$.
Eq. D19	$r = A_1/(A_1 + A_2)$	Defined ratio of coefficients.

APPENDIX C: QUANTITATIVE IMAGING PROTOCOLS (EXAMPLE FORMATS)

1. Conjugate View Imaging—Planar Views

The steps involved in activity quantitation based on transmission conjugate-view planar imaging are as follows:

1. Determine the transmission factor, $\mathcal{T} (= e^{-\mu t})$, through each source ROI. Usually the transmission factor is measured before administering the radiopharmaceutical to the patient, but it may also be determined after administration. To measure the transmission factor, prepare a source of activity whose surface area is greater than that of the source region with the same radionuclide as that to be used for the patient imaging study. As an example, for small regions fill the bottom of a Petri dish (covered and sealed to prevent possible contamination); for large regions, fill a flood source. Count the transmission source for a fixed time (e.g., 5 min) through the patient across the area of the specific body regions of interest and again in air at the same source-to-collimator distance. Another method for acquiring transmission data is through a whole-body transmission scan which may be performed with a line or flood source. The transmission factor is calculated as $\mathcal{T} = I/I_0$, where I is the count rate (cpm) obtained with the transmission source viewed through the patient and I_0 is the count rate obtained with the transmission source in air. The count rates are obtained by drawing appropriate ROIs encompassing the source region. The measurement of the transmission factor is thus based on relative counts with and without the patient. If the transmission factor is determined postadministration, a separate measurement of activity in the region at that time must be obtained. In this case, $\mathcal{T} = (I - I_{pt})/I_0$, where I_{pt} is the count rate obtained with the patient alone;
2. Obtain the imaging system calibration factor, C, by preparing a standard of known activity, usually 37–74 MBq (1–2 mCi), in a suitable container of the same radionuclide to be used for patient administration. Count this standard in air for a fixed time (e.g., 5 min) at a source-to-collimator distance that approximates that of the patient midline distance used for the

imaging study. The count rate per unit activity (cpm/MBq) represents the calibration factor. The collimator count-rate response as a function of the source-to-collimator distance must be known. For parallel-hole collimators, collimator efficiency is invariant; however, for other collimators, such as diverging, converging and pinhole collimators, the efficiency is dependent upon distance;

3. Acquire anterior and posterior views of each source ROI for a fixed time (or for a fixed number of counts which must be normalized to unit count time for each of the conjugate views);
4. Determine the anterior I_A and posterior I_P conjugate-view count rates for the region to be quantitated through ROI analysis. Choose an appropriate background correction technique if required as described in the Section IV.A.2.b. For the simple background subtraction method, the adjacent ROIs are usually drawn contiguous to the region ROI and may be normalized to the area of the organ region if a different size ROI is used for I_{ADJ} versus I_A and I_P . Care should be taken to avoid high and/or low activity areas for selection of the background ROI; and
5. Determine the absolute activity, A (MBq), in each region. For example, for simple background subtraction, per Eqs. 1 and 6:

$$A = F \sqrt{\frac{I_A I_P}{\mathcal{T}}} \times \frac{f}{C}, \quad \text{Eq. C1}$$

where F is the background correction factor and f provides the correction for the source region attenuation and source thickness (see Eqs. 2 and 6 or 7). In most cases, f will be approximately equal to unity. If the ROI is small and the variation in body thickness within the ROI is also small, this equation can be used to calculate the activity for the entire ROI. On the other hand, if the ROI is large (e.g., encompasses the entire liver), a pixel-by-pixel calculation may have to be made.

A conjugate-view measurement is not necessary at each of the time points chosen for generating ROIs unless the distribution of the activity is time-dependent. (This occurs, for example, in the

stomach when a radiolabeled meal redistributes anteriorly from the fundus to the antrum.) For the static distribution situation, serial anterior or posterior ROI count rates can be used to establish the temporal count rate dependence of the source region. For at least one of these selected imaging time points, a conjugate-view measurement of the source region is required to convert the anterior or posterior count rates in these ROIs to absolute activity and, thus, provide a source region conversion factor. This source region conversion factor can be applied to all anterior or posterior count rate measurements for this region of interest to provide the quantitative time-activity data.

2. SPECT Imaging

The steps involved in activity quantitation based on SPECT imaging are as follows:

1. Acquire a SPECT study of each source region (e.g. chest SPECT for lungs, abdominal SPECT for liver and spleen and pelvic SPECT for sacrum). A typical SPECT study is acquired in a 64×64 image matrix for 64 projections over 360° for 20 sec per projection using the body contour rotation mode;
2. Reconstruct the raw data by filtered backprojection using a commercially available filter (e.g., Butterworth or Ramp-Hanning) in the transaxial, sagittal and coronal planes. Apply Chang's method of attenuation correction to the transverse reconstructed slices using a linear attenuation coefficient appropriately chosen to compensate for the added counts due to Compton scatter (e.g., 0.12 cm^{-1} for ^{99m}Tc);
3. Obtain the imaging system calibration factor by preparing a standard of known activity, usually 37–74 MBq (1–2 mCi), in a point or line source of the same radionuclide used in the patient and acquire a SPECT study using the same radius of rotation as the patient study. Reconstruct with the same algorithm as in the patient study except omit the attenuation correction since the calibration source is imaged in air. Using the same threshold as in the patient study in Step 4 below, determine the count rate per unit activity calibration factor (cpm/MBq) by dividing the total reconstructed counts exceeding the threshold by the product of the known activity with the SPECT acquisition time; and
4. Determine the source region activity using a fixed threshold method. Search through all the reconstructed slices spanning the object to find the maximum voxel count. Only voxels containing counts greater than a phantom-determined threshold value will be subsequently included in the activity calculation. The source region is again searched through all the selected slices, this time only including voxels with counts greater than the threshold value. The activity (MBq) is then determined from the sum of the counts in the included voxels divided by the acquisition time and the independently acquired count rate per unit activity system calibration factor (cpm/MBq).

A more comprehensive protocol for SPECT activity determination would compensate for added counts from scatter that is independent of the attenuation correction. Such a protocol should result in more accurate SPECT data. A practical procedure to carry out the compensation involves two or perhaps three energy windows. One window is the standard energy window for the photopeak of the administered radionuclide. The second is placed at a lower energy to monitor scattering. A third window at an energy above the photopeak is needed for radionuclides such as ^{131}I to monitor collimator septal penetration. For the two-window situation, acquire a SPECT study as in Step 1 using two energy windows. A phantom-determined fraction of the counts in the lower energy window is subtracted from the

photopeak counts to correct for scattered photons present in the photopeak window. This subtraction should be carried out for each pixel, projection by projection. The subtracted image set is then reconstructed and analyzed according to Steps 2–4 above except for two modifications: (a) the narrow beam geometry attenuation coefficient is used for attenuation correction (e.g., 0.15 cm^{-1} for ^{99m}Tc); and (b) the calibration factor and the fraction of the lower-energy window count needed for subtraction are determined from the same phantom measurement in which the standard of known activity is placed within a water-filled cylinder. Two separate phantom studies are required, each using a different activity amount to determine both the calibration factor and subtraction fraction (i.e., the two independent equations can be solved uniquely for the two unknown parameters).

3. PET Imaging

The steps involved in activity quantitation based on PET imaging are as follows:

1. Perform a patient transmission scan prior to administration of the radiopharmaceutical. Use a ring source of any appropriate and available positron emitter. Calculate a multiplicative attenuation correction factor for each ray and apply it to the projection data (sinogram);
2. Acquire a PET study of each source region and apply appropriate corrections for accidental coincidences, detector sensitivities, dead time and attenuation.
3. Obtain the imaging system calibration factor by preparing a standard of known activity in a suitable container (e.g., cylindrical phantom) of the same radionuclide to be used for patient administration and performing a PET study as in Steps 1–2.
4. Reconstruct the patient images and use a thresholding method as described in the SPECT protocol to determine the source region activity.

APPENDIX D: TEMPORAL SAMPLING ERROR ANALYSIS

1. Assessment of Errors When Uptake is Noninstantaneous

The uptake and retention of a compound in any given tissue often can be simulated as a biexponential function of time (Eq. D1), i.e., a curve with an uptake and monophasic washout. In this simulation, the fractional activity in the region, A_h , is predicted to rise from zero, at $t = 0$, to some value and then fall off as the activity washes out:

$$A_h(t) = A_2 e^{-(\lambda + \lambda_2)t} - A_1 e^{-(\lambda + \lambda_1)t}, \quad \text{Eq. D1}$$

where $A_1 = A_2$; $\lambda_1 =$ biologic uptake constant (hr^{-1}); $\lambda_2 =$ biologic disappearance constant (hr^{-1}); and $\lambda =$ physical decay constant (hr^{-1}).

As indicated, the coefficients A_1 and A_2 are equal and of opposite sign, which indicates that the activity in the region started at zero, increased to some fraction of the administered activity with an effective half-time $T_{e1} = 0.693/(\lambda + \lambda_1)$ and was removed with an effective half-time of $T_{e2} = 0.693/(\lambda + \lambda_2)$. The residence time, τ_h , is given by:

$$\tau_h = 1.443[A_2 T_{e2} - A_1 T_{e1}]. \quad \text{Eq. D2}$$

If it is assumed that the uptake is instantaneous, the uptake rate λ_1 is infinite, i.e., $T_{e1} = 0$, then Eq. D1 reduces to:

$$A_{\text{inst}}(t) = A_2 e^{-(\lambda + \lambda_2)t}. \quad \text{Eq. D3}$$

The residence time is:

$$\tau_{\text{inst}} = 1.443 A_2 T_{e2} \quad \text{Eq. D4}$$

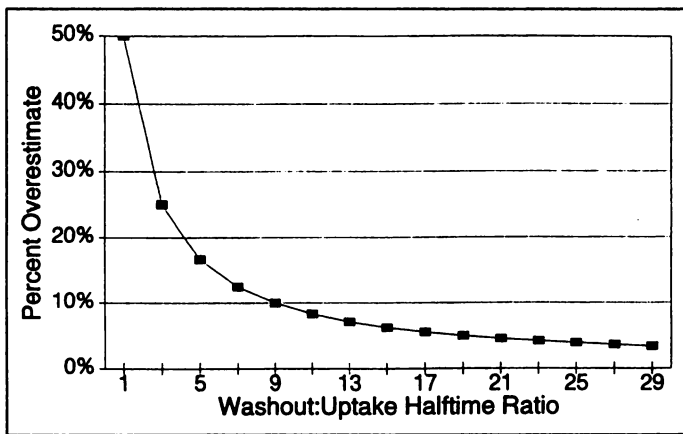


FIGURE D1. Percentage error (overestimation) in residence time calculations when a source region's peak uptake does not occur instantaneously. As the ratio of the effective washout half-time to the neglected uptake effective half-time approaches unity, i.e., $T_{e2} \approx T_{e1}$, the errors caused by neglecting the noninstantaneous uptake dramatically increase. In cases where the uptake effective half-time is $<5\%$ of the value of the washout effective half-time, the errors are essentially negligible.

The fractional error in the residence time calculations under the instantaneous uptake approximation, k , can be defined as equal to $(\tau_{inst} - \tau)/\tau$. Using Equations D2 and D4, k may be rewritten as:

$$k = T_{e1}/[T_{e2} - T_{e1}]. \quad \text{Eq. D5}$$

This result is obtained by dividing the difference between Equations D5 and D2 by Equation D2.

Neglecting the uptake phase causes an overestimate of the residence time because τ_{inst} is larger than τ . Figure D1 shows how the percentage error varies as a function of the relative magnitude of the washout effective half-time compared to the uptake effective half-time. Percentage errors of $>20\%$ are obtained when the washout-to-uptake half-time ratio is <6 . For example, if the uptake and washout effective half-times are 5 and 35 hr, respectively, their ratio is 1:7. Thus, if the uptake phase is neglected in this case, Figure D1 indicates that the residence time would be overestimated by $\sim 17\%$.

A direct result of Eq. D5 is that for a given value of k , the uptake effective half-time is equal to the washout effective half-time multiplied by $k/(k + 1)$, i.e.:

$$T_{e1} = T_{e2}k/(k + 1). \quad \text{Eq. D6}$$

It can be inferred from Eq. D6 that, for small percentage errors, $T_{e1} = kT_{e2}$.

To determine the earliest time necessary for sampling the activity while keeping the percentage error from neglecting the uptake phase to a minimum, the time (t_{max}) at which the time-activity equation is maximized must be determined. The initial activity determination should be performed at this time point to minimize the errors associated with mischaracterizing the uptake phase. This is found by taking the derivative of Eq. D1 with respect to time, setting it equal to 0 and solving for t_{max} :

$$t_{max} = 1.443kT_{e2} \ln(k + 1)/(k). \quad \text{Eq. D7}$$

Figure D2 shows the variation of t_{max} (the time for initial sampling that constrains the error to $<k\%$) as a function of effective washout half-time (T_{e2}) for four different values of percentage error ($<10\%$) in residence time estimates. To use this figure, find the appropriate T_{e2} , decide on the acceptable error, and then find the y-intercept (t_{max}) that satisfies these conditions. From Figure D2, for an effective washout half-time of 50 hr, sampling is necessary before 10 hr postadministration (t_{max}) to keep the error below 5% as a result of neglecting the uptake phase.

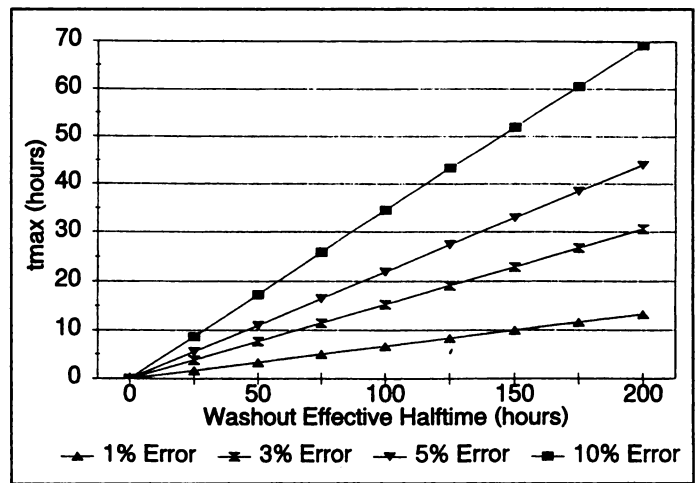


FIGURE D2. T_{max} , the time to peak uptake in a source region, is the latest time for which activity retention should be determined in order to ensure that the error in residence time determination is kept below a specified value (1%–10%). One can also estimate the error introduced when the uptake phase is neglected. For example, assume the washout half-time for an ^{131}I -labeled compound is 100 hr and the initial activity determination occurs 24 hr postadministration. The error in the source region residence time would then be $\sim 7\%$.

2. Washout Phase Error Assessment

The washout phase in a given tissue can again be simulated as a biexponential function of time (Eq. D8). In the following example, it is also assumed that an insignificant error is being made by assuming instantaneous uptake in the tissue:

$$A_h(t) = A_1e^{-(\lambda + \lambda_1)t} + A_2e^{-(\lambda + \lambda_2)t}, \quad \text{Eq. D8}$$

where $A_1 \neq A_2$; λ_1 = biologic disappearance constant for rapid washout component (hr^{-1}); λ_2 = biologic disappearance constant for slow washout component (hr^{-1}); T_{e1} = effective half-time (hr) for rapid washout = $0.693/(\lambda + \lambda_1)$; and T_{e2} = effective half-time (hr) for slow washout = $0.693/(\lambda + \lambda_2)$. In this example, the pre-exponential coefficients will be normalized to unity, i.e., $A_2 = 1 - A_1$ for the case of a single source region. In general, for a given region $\sum_i A_{hi} \neq 1$ if there is uptake in other regions.

In this case, the residence time is given by:

$$\tau = 1.443[A_1T_{e1} + A_2T_{e2}]. \quad \text{Eq. D9}$$

As an example, assume that only data that describe the long-term activity retention in tissue is acquired and no data were obtained at earlier times. In this simulation, the estimated initial activity is equal to A_2 , the fractional activity associated with the effective half-time of the long-term removal, T_{e2} :

$$A_{long}(t) = A_2e^{-(\lambda + \lambda_2)t}, \quad \text{Eq. D10}$$

where its associated residence time is given by:

$$\tau_{long} = 1.443A_2T_{e2}. \quad \text{Eq. D11}$$

Equations D9 and D11 can be rewritten as follows:

$$\tau/(A_2T_{e2}) = 1.443 \cdot [1 + A_1T_{e1}/(A_2T_{e2})] \quad \text{Eq. D12}$$

and

$$\tau_{long}/(A_2T_{e2}) = 1.443. \quad \text{Eq. D13}$$

As before, the fractional error in the residence time calculations is defined as the ratio of the difference between τ and τ_{long} to τ . This result (Eq. D14) is obtained by dividing the difference between Equations D12 and D13 by Equation D12:

$$k = \{A_1T_{e1}/(A_2T_{e2})\} / [1 + A_1T_{e1}/(A_2T_{e2})]. \quad \text{Eq. D14}$$

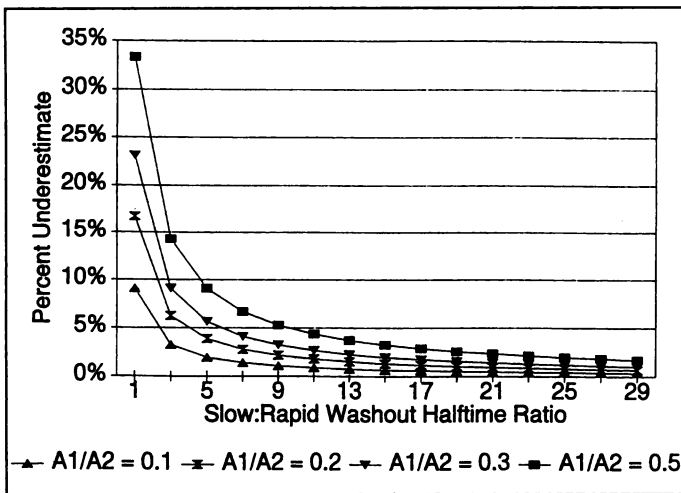


FIGURE D3. Error in residence time calculation when the rapid washout phase is neglected. For source regions exhibiting biphasic clearance, the magnitude of the residence time underestimate (when neglecting the rapid washout component) are functions of the ratio of the slow to rapid washout effective half-times (T_{e2}/T_{e1}) and the ratio of the fractional activity removed rapidly to that removed slowly (A_1/A_2). When the relative amount of activity rapidly removed from the region is small compared to the long-term retention component, the errors due to neglecting the rapid washout are minor. As the long-term retention component effective half-time becomes much larger than that of the rapidly removed component, the errors are minor regardless of how the activity was distributed between the two washout components. The foregoing does not account for errors in residence time determination due to neglecting noninstantaneous uptake.

Figure D3 shows how the percentage error resulting from neglect of the rapid washout component varies as a function of the relative magnitude of the slow washout effective half-time compared to the rapid washout effective half-time. Two general trends should be noted. First, the larger the fraction of activity associated with the initial rapid removal effective half-time, the larger the percentage error. Also, the smaller the ratio of the slow washout effective removal half-time, T_{e2} , relative to T_{e1} , the larger the percentage error. To illustrate, assume a radiopharmaceutical exhibits biexponential washout where 10 kBq is removed with an effective half-time of 2 hr and 50 kBq is removed with an effective half-time of 10 hr. Therefore, $A_1/A_2 = 0.2$ and $T_{e2}/T_{e1} = 5$. According to Figure D3, the error in neglecting the rapid washout component is $\sim 4\%$.

3. Assessment of Errors for Long-Term Retention of Activity

The actual activity retention function can again be described by Equation D8 and the associated residence time by Equation D9. In this case assume that samples are not obtained at later times and only data that describe the early or rapid washout from the tissue are acquired. The resulting derived retention function is given by Equation D15. Note that the estimated initial activity is equal to the sum of the individual activity fractions for both the rapid and slow washout components:

$$A_{\text{rapid}}(t) = (A_1 + A_2)e^{-(\lambda + \lambda_j)t} \quad \text{Eq. D15}$$

The associated residence time is given by:

$$\tau_{\text{rapid}} = 1.443(A_1 + A_2)T_{e1} \quad \text{Eq. D16}$$

Eqs. D9 and D16 can be rewritten as follows:

$$\tau / \{T_{e1}(A_1 + A_2)\} = 1.443[r + (1 - r)T_{e2}/T_{e1}] \quad \text{Eq. D17}$$

and

$$\tau_{\text{rapid}} / \{T_{e1}(A_1 + A_2)\} = 1.443, \quad \text{Eq. D18}$$

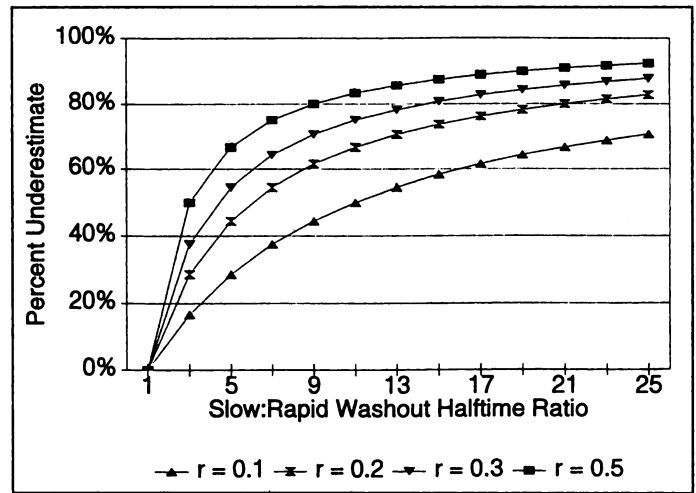


FIGURE D4. Potential errors in source region determination when the long-term retention is neglected. The ratio of activity removed from the source region to the total uptake is r , where $r = A_1/(A_1 + A_2)$. $(1 - r)$ is equal to the fraction of the activity retained with a long effective removal half-time. It is clear from this figure that not determining the long-term retention component introduces large errors (underestimates) in the source region residence time calculations.

where

$$r = A_1/(A_1 + A_2) \quad \text{Eq. D19}$$

$$1 - r = A_2/(A_1 + A_2) \quad \text{Eq. D20}$$

The fractional error in the residence time calculations, k , can be defined, as before, as the ratio of the difference between τ and τ_{rapid} to τ . This result (Eq. D19) is obtained by dividing the difference between Equations D17 and D18 by Equation D17:

$$k = \{[r + (1 - r)T_{e2}/T_{e1}] - 1\} / [r + (1 - r)T_{e2}/T_{e1}] \quad \text{Eq. D21}$$

Figure D4 shows how the percentage error from neglecting the long-term retention of activity phase or the slow washout component varies as a function of the relative magnitude of the slow washout effective half-time compared to the rapid effective washout half-time. The percentage error is very sensitive to two variables, namely r and the ratio of T_{e2}/T_{e1} . The smaller the fraction of activity associated with the rapid effective half-time, r , the larger the percentage error. Also, the larger the effective half-time for slow washout, T_{e2} , relative to T_{e1} , the larger the percentage error. For example, assume the radiolabeled compound is 30% removed with an effective half-time of 2 hr and is 70% removed with an effective half-time of 10 hr. Then $r = 0.3$ and $T_{e2}/T_{e1} = 5$. According to Figure D4, the error in neglecting the long-term washout component is $\sim 45\%$.

APPENDIX E: CALCULATIONAL EXAMPLES

1. Instantaneous Uptake: No Biologic Removal

Problem. Consider 10 mCi of a ^{11}C -labeled compound that is taken up rapidly and distributes uniformly in the whole body (WB). Assume that no biologic removal occurs. The physical half-life of ^{11}C is 0.34 hr. Calculate the cumulated activity and residence time in the whole body.

Solution. The activity in the whole body is removed exponentially with a half-time equal to the physical half-life T . From Eq. 24, one obtains:

$$A_{\text{WB}}(t) = \sum_j A_j(0)e^{-(\lambda + \lambda_j)t} = A_0e^{-\lambda t} = A_0e^{-0.693t/T},$$

where $A_{\text{WB}}(t)$ is the activity in the whole body at time t , λ is the physical decay constant, λ_j is the biologic disappearance constant,

TABLE E1
Cumulated Activity and Residence Time in the Stomach

Time (hr)	Net cpm	Activity (μCi)
0	100,000	500
0.5	51,358	257
1.0	26,376	132
1.5	13,546	67.7
2.0	6,957	34.8
2.5	3,573	19.9
3.0	1,835	9.2

TABLE E2
Cumulated Activity in the Kidneys

Time (sec)	Counts in 20 sec		Activity in kidneys (μCi)
	A/P left kidney	A/P right kidney	
20	41,070/47,231	32,360/37,214	54.6
60	90,860/104,489	84,730/97,439	130
160	145,570/167,405	143,230/164,714	215
240	150,140/172,660	161,790/186,058	232
280	141,630/162,874	166,650/191,647	229
440	94,600/108,790	150,000/172,500	182
580	73,690/84,744	125,050/143,807	148
720	58,810/67,631	92,610/106,501	112
860	45,760/52,624	76,770/88,285	91.0
940	42,240/48,576	62,870/72,300	78.1
1060	36,490/41,964	52,820/60,743	66.4
1200	30,700/35,305	42,480/48,852	54.4

A_0 is the administered activity and T is the physical half-life. Note that because there is instantaneous uptake and no biologic removal, $A_{WB}(t)$ has only a single exponential term with $\lambda_j = 0$. The cumulated activity in the whole body is the area under the whole body activity-time curve generated from the $A_{WB}(t)$ function above. According to Eq. 25, the cumulated activity for complete decay is given by:

$$\begin{aligned} \tilde{A}_{WB} &= \int_0^{\infty} A_{WB}(t) dt = A_0 \int_0^{\infty} e^{-0.693t/T} dt = 1.443A_0T \\ &= 1.443(10,000 \mu\text{Ci})(0.34 \text{ hr}) = 4,900 \mu\text{Ci} \cdot \text{hr}. \end{aligned}$$

The residence time is:

$$\tau_{WB} = \tilde{A}_{WB}/A_0 = (4,900 \mu\text{Ci} \cdot \text{hr})/(10,000 \mu\text{Ci}) = 0.49 \text{ hr}.$$

2. Instantaneous Uptake Removal by Both Physical Decay and Biologic Elimination

Problem. To measure the gastric emptying rate for liquids, a patient is instructed to drink 300 ml of water containing 500 μCi of $^{113\text{m}}\text{In}$ -DTPA. Planar images of the stomach (S) are obtained at 30 minute intervals for three hours. The net counts per minute (cpm) in the stomach region after subtracting background, if present, are given in Table E1. The physical half-life of $^{113\text{m}}\text{In}$ is 1.658 hr. Calculate the cumulated activity and residence time in the stomach (Table E1).

Solution. Because all of the activity is in the stomach at $t = 0$ (instantaneous uptake), the activity in the stomach at this time is A_0 , where A_0 is the administered activity. At all other times, the activity in the stomach at time t is given by $A_S(t) = A_0 [\text{cpm}(t)/\text{cpm}(t = 0)]$. These data, shown in Table E1, have not been corrected for physical decay and, therefore, represent the effective removal of activity from the stomach. If these time-activity data were plotted on graph paper it would be observed that the activity is removed from the stomach in a manner corresponding to a single-component exponential clearance. From Eq. 24, one obtains:

$$A_S(t) = \sum_j A_j(0)e^{-(\lambda + \lambda_j)t} = A_0 e^{-\lambda_e t} = A_0 e^{-0.693t/T_e},$$

where $A_S(t)$ is the activity in the stomach at time t , λ is the physical decay constant, λ_j is the biologic disappearance constant, λ_e is the effective disappearance constant, A_0 is the administered activity and T_e is the effective half-time. A least squares fit to these activity-time data indicates an effective half-time of 0.52 hr. According to Eq. 25, the cumulated activity in the stomach can now be calculated as:

$$\begin{aligned} \tilde{A}_S &= \int_0^{\infty} A_S(t) dt = A_0 \int_0^{\infty} e^{-0.693t/T_e} dt = 1.443A_0T_e \\ &= 1.443(500 \mu\text{Ci})(0.52 \text{ hr}) = 375 \mu\text{Ci} \cdot \text{hr}. \end{aligned}$$

The residence time in the stomach is:

$$\tau_S = \tilde{A}_S/A_0 = (375 \mu\text{Ci} \cdot \text{hr})/(500 \mu\text{Ci}) = 0.75 \text{ hr}.$$

3. Noninstantaneous Uptake: Removal By Both Physical Decay and Biologic Elimination

Problem. A patient is administered 37 MBq (1 mCi) of $^{99\text{m}}\text{Tc}$ -MAG3. Conjugate planar gamma camera images of the kidneys are acquired for 20 sec at various times post administration. The counts in the anterior (A) and posterior (P) views of the left and right kidney (K) ROIs are given in Table E2. The physical half-life of $^{99\text{m}}\text{Tc}$ is 6 hr, the transmission factor through the kidneys is 0.75, and the imaging system calibration factor is 5000 cpm/ μCi . Assume that the kidney correction factor, f , is equal to unity. Calculate the cumulated activity in the kidneys (Table E2).

Solution. The total activity in the two kidneys can be calculated using Eq. 1 and is given in Table E2. If these time-activity data were plotted on graph paper it would be observed that the retention of activity from the kidneys can be described by a three-component exponential function with a single term for the uptake phase and two terms for the clearance phase. Therefore, the kidney activity can be described by:

$$\begin{aligned} A_K(t) &= \sum_j A_j(0)e^{-(\lambda + \lambda_j)t} = \sum_j A_j(0)e^{-(\lambda_j)t} \\ &= A_1(0)e^{-(\lambda_1)t} + A_2(0)e^{-(\lambda_2)t} - A_3(0)e^{-(\lambda_3)t}. \end{aligned}$$

A least squares fit to the $A_K(t)$ function above results in:

$$A_K(t) = 167e^{-3.68t} + 933e^{-15.2t} - 1100e^{-22.8t},$$

where the coefficients are in μCi and the effective half-time constants are in hr^{-1} . Note that the coefficient corresponding to the uptake phase (A_3) is negative and that $A_3 = -(A_1 + A_2)$. The cumulated activity in the kidneys can now be calculated as:

$$\begin{aligned} \tilde{A}_K &= \int_0^{\infty} A_K(t) dt = \sum_j A_j/\lambda_j \\ &= \frac{167}{3.68} + \frac{933}{15.2} - \frac{1100}{22.8} = 58.5 \mu\text{Ci} \cdot \text{hr}. \end{aligned}$$

4. Curve Fitting: Least Squares and Trapezoidal Methods

Problem. A compound labeled with 100 μCi of $^{90\text{Y}}$ distributes uniformly in the whole body. Determine the cumulated activity and residence time in the whole body using both the trapezoidal and least squares methods. The following data show the whole-body retention at various times (Table E3).

TABLE E3
Whole-Body Retention at Various Times

Time (hr)	Activity (μCi)
0	100
0.5	72
1	35
2	24
4	20
6	15
10	12

Solution. To determine \tilde{A} , we integrate the time–activity curve shown in Figure E1.

The simplest way to do this is to calculate the area under the curve through the observed data points numerically; each of the six intervals (0–0.5 hr, 0.5–1 hr, 1–2 hr, 2–4 hr, 4–6 hr and 6–10 hr) is treated separately by creating trapezoidal areas and the parts are then added:

$$\tilde{A}_1 = (100 + 72)/2 \mu\text{Ci} \times 0.5 \text{ hr} = 43 \mu\text{Ci} \cdot \text{hr}$$

$$\tilde{A}_2 = (72 + 35)/2 \mu\text{Ci} \times 0.5 \text{ hr} = 26.75 \mu\text{Ci} \cdot \text{hr}$$

$$\tilde{A}_3 = (35 + 24)/2 \mu\text{Ci} \times 1.0 \text{ hr} = 29.5 \mu\text{Ci} \cdot \text{hr}$$

$$\tilde{A}_4 = (24 + 20)/2 \mu\text{Ci} \times 2.0 \text{ hr} = 44 \mu\text{Ci} \cdot \text{hr}$$

$$\tilde{A}_5 = (20 + 15)/2 \mu\text{Ci} \times 2.0 \text{ hr} = 35 \mu\text{Ci} \cdot \text{hr}$$

$$\tilde{A}_6 = (15 + 12)/2 \mu\text{Ci} \times 4.0 \text{ hr} = 54 \mu\text{Ci} \cdot \text{hr}$$

$$\text{Total} = 232 \mu\text{Ci} \cdot \text{hr}$$

However, we must still account for the remaining area under the curve after 10 hr. Because we have no data to describe further removal from the body, a conservative approach is to assume that, after 10 hr, the only removal of the remaining 12 μCi is by radioactive decay. This remaining area (\tilde{A}_7) may be calculated analytically (for ^{90}Y , $\lambda = 0.693/64 \text{ hr} = 0.0108 \text{ hr}^{-1}$):

$$\tilde{A}_7 = \int_t^\infty A(10)e^{-\lambda t} dt = 12 \mu\text{Ci} \int_{10}^\infty e^{-0.0108t} dt = 997 \mu\text{Ci} \cdot \text{hr}.$$

So the total area under the curve predicted by this method is 1230 $\mu\text{Ci} \cdot \text{hr}$, and τ is equal to 12.3 hr.

A preferable method for integrating under the curve may be to use a least squares technique to fit the data with a mathematical

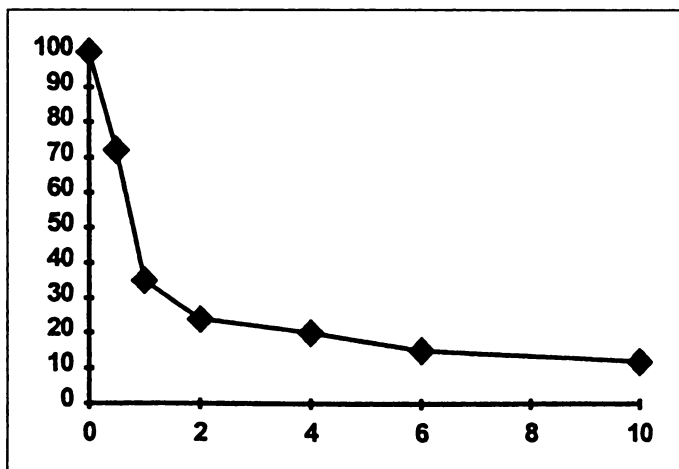


FIGURE E1. Time–activity curve from data in Table E3.

function, which can then be integrated analytically. For the example above, curve stripping gives a biexponential function, and a least squares fit will yield the following equation:

$$A(t) = 18.6e^{-0.039t} + 81.4e^{-1.23t}.$$

Note that the sum of the coefficients of the two exponential terms is equal to the administered activity of 100 μCi . By integrating the least squares equation to time $t = 10 \text{ hr}$ and comparing the result with the estimate generated by the trapezoidal method, a reasonable agreement is achieved:

$$\begin{aligned} \tilde{A} &= 18.6/0.039 \times [1 - e^{-0.039 \times 10}] + 81.4/1.23 \times [1 - e^{-1.23 \times 10}] \\ &= 220 \mu\text{Ci} \cdot \text{hr}. \end{aligned}$$

This shows that the trapezoidal method provides a satisfactory approximation to the area under the curve over the observed data set.

If we now integrate from 0 to infinity, the cumulated activity becomes:

$$\tilde{A} = 18.6/0.039 + 81.4/1.23 = 477 + 66 = 543 \mu\text{Ci} \cdot \text{hr},$$

and τ is equal to 5.43 hr.

This estimate does not agree well with that from the trapezoidal method. The reason for this is that the trapezoidal method made the conservative assumption that removal from the body is only by physical decay after 10 hr, whereas the least squares method assumes that the effective half-time of 17.8 hr continues after the end of the data set. If no assumption is made concerning activity retention following the last data point, the trapezoidal method out to that point will underestimate \tilde{A} .

REFERENCES

- Loevinger R, Berman M. *A revised schema for calculating the absorbed dose from biologically distributed radionuclides*, MIRD Pamphlet No. 1 Revised. New York: The Society of Nuclear Medicine; 1976.
- Loevinger R, Budinger TF, Watson EE. *MIRD primer for absorbed dose calculations*, Revised Edition. New York: The Society of Nuclear Medicine; 1991.
- Langmuir VK, Fowler JF, Knox SJ, Wessels BW, Sutherland RM, Wong JYC. Radiobiology of radiolabeled antibody therapy as applied to tumor dosimetry. *Med Phys* 1993;20:601–610.
- Bolch WE, Bouchet LG, Robertson JS, et al. MIRD Pamphlet No. 17: the dosimetry of nonuniform activity distribution—radionuclide values at the voxel level. *J Nucl Med* 1999;40(1):11S–36S.
- Foster DM, Boston RC. The use of computers in compartmental analysis: the SAAM and CONSAM programs. In: Robertson JS, Colombetti LG, eds. *Compartmental distribution of radiotracers*. Boca Raton, FL: CRC Press; 1983:73–142.
- Bogen DK. Simulation software for the Macintosh. *Science* 1989;246:138–142.
- Ralston ML, Jennrich RI, Sampson PF, Uno FK. *Fitting pharmacokinetic models with BMDPAR*, BMDP Technical Report No. 58. Los Angeles: UCLA Health Sciences Computing Facilities; 1979.
- Leichner PK, Koral KF, Jaszczak RJ, Green AJ, Chen GTY, Roeske JC. An overview of imaging techniques and physical aspects of treatment planning in radioimmunotherapy. *Med Phys* 1993;20:569–577.
- Thomas SR, Maxon HR, Kereiakes JG. In vivo quantitation of lesion radioactivity using external counting methods. *Med Phys* 1976;3:253–255.
- Landaw EM, DiStefano JJ. Multiexponential, multicompartmental, and noncompartmental modeling. II. Data analysis and statistical considerations. *Am J Physiol* 1984;246:R665–R677.
- Wessels BW, Breitz H, Mills G, Siegel J, Stabin M. The 10th international conference on monoclonal antibody immunoconjugates for cancer: radiodosimetry and radiopharmaceuticals for therapy. *Cancer Biother Radiopharm* 1996;11:25–42.
- Code of Federal Regulations, Title 21, Part 20. Food and Drugs (21CFR312.23.10.ii). Washington: U.S. Government Printing Office, revised April 1, 1989:73.
- Fleming JS. A technique for the absolute measurement of activity using a gamma camera and computer. *Phys Med Biol* 1979;24:176–180.
- Macey DJ, Marshall R. Absolute quantitation of radiotracer uptake in the lungs using a gamma camera. *J Nucl Med* 1982;23:731–734.
- Tsui BMW, Chen C-T, Yasillo NJ, et al. A whole-body scanning system for collection of quantitative in vivo distribution data in humans. In: Watson EE, Schlafke-Stelson AT, Coffey JL, et al., eds. *Third international radiopharmaceutical dosimetry symposium: proceedings of a conference held at Oak Ridge, TN, October 7–10, 1980*, HHS Publication FDA 81-8160. Rockville, MD: U.S. Dept. Health and Human Services; 1981:138.
- Thomas SR, Maxon RH, Kereiakes JG. Techniques for quantitation of in vivo radioactivity. In: Gelfand MJ, Thomas SR, eds. *Effective use of computers in nuclear medicine*. New York: McGraw-Hill; 1988:468–484.

17. Kojima M, Takaki Y, Matsumoto M, et al. A preliminary phantom study on a proposed model for quantification of renal planar scintigraphy. *Med Phys* 1993;20:33-37.
18. Rohe RC, Thomas SR, Stabin MG, et al. Biokinetics and dosimetry analysis in healthy volunteers for a two-injection (rest-stress) protocol of the myocardial perfusion imaging agent ^{99m}Tc -Q3. *J Nucl Cardiol* 1995;2:395-404.
19. International Commission on Radiation Protection. *Report of the task group on reference man*, ICRP Publ. No. 23. New York: Pergamon Press; 1975:103-140.
20. Thomas SR, Gelfand MJ, Burns GS, et al. Radiation absorbed-dose estimates for the liver, spleen, and metaphyseal growth complexes in children undergoing gallium-67 citrate scanning. *Radiology* 1983;146:817-820.
21. Wu RK, Siegel JA. Absolute quantitation of radioactivity using the buildup factor. *Med Phys* 1984;11:189-192.
22. Siegel JA, Wu RK, Maurer AH. The buildup factor: effect of scatter on absolute volume determination. *J Nucl Med* 26:390-394, 1985.
23. Siegel JA. The effect of source size on the buildup factor calculation of absolute volume. *J Nucl Med* 26:1319-1322, 1985.
24. Van Rensburg AJ, Lotter MG, Heyns AP, et al. An evaluation of four methods of ^{111}In planar image quantitation. *Med Phys* 1988;15:853-861.
25. Jaszczak RJ, Floyd CE, Coleman RE. Scatter compensation techniques for SPECT. *IEEE Trans Nucl Sci* 1985;32:786-793.
26. Koral KF, Clinthorne NH, Rogers WL. Improving emission-computed tomography quantification by Compton-scatter rejection through offset windows. *Nucl Inst Methods Phys Res* 1986;A242:610-614.
27. Pretorius PH, Van Rensburg AJ, Van Assswegen, et al. The channel ratio method of scatter correction for radionuclide image quantitation. *J Nucl Med* 1993;34:330-335.
28. King MA, Hademenon GJ, Glick SJ. A dual-photopeak window method for scatter correction. *J Nucl Med* 1992;33:605-612.
29. Ogawa K, Harata Y, Ichihara T, Kubo A, Hashimoto S. A practical method for position-dependent Compton-scatter correction in single emission CT. *IEEE Trans Med Imag* 1991;10:408-412.
30. Macey DA, Grant EF, Bayouth JE, et al. Improved conjugate view quantitation of I-131 by subtraction of scatter and septal penetration events with a triple energy window method. *Med Phys* 1995;22:1637-1643.
31. King MA, Doherty PW, Schwinger RB. A Wiener filter for nuclear medicine images. *Med Phys* 1983;10:876-880.
32. King MA, Schwinger PW, Doherty PW, Penney BC. Two-dimensional filtering of SPECT images using the Metz and Wiener filters. *J Nucl Med* 1984;25:1234-1240.
33. Penney BC, Glick SJ, King MA. Relative importance of the error success in Wiener restoration of scintigrams. *IEEE Trans Med Imag* 1990;9:60-70.
34. Clarke LP, Cullom SJ, Shaw R, et al. Bremsstrahlung imaging using the gamma camera: factors affecting attenuation. *J Nucl Med* 1992;33:161-166.
35. Shen S, DeNardo GL, DeNardo S. Quantitative bremsstrahlung imaging of yttrium-90 using a Wiener filter. *Med Phys* 1994;21:1409.
36. Halama, JR, Henkin RE, Friend LE. Gamma camera radionuclide images: improved contrast with energy-weighted acquisition. *Radiology* 1988;169:533-538.
37. DeVito RP, Hamill JJ, Treffert J, Staub EW. Energy-weighted acquisition of scintigraphic images using finite spatial filters. *J Nucl Med* 1989;30:2029-2035.
38. Hamill, JJ, DeVito RP. Scatter reduction with energy-weighted acquisition. *IEEE Trans Nucl Sci* 1989;NS-36:1334-1339.
39. DeVito RP, Hamill JJ. Determination of weighting functions for energy-weighted acquisition. *J Nucl Med* 1991;32:343-349.
40. Breitz HB, Fisher DR, Weiden PL, et al. Dosimetry of rhenium-186-labeled monoclonal antibodies: methods, prediction from technetium-99m-labeled antibodies and results of Phase I trials. *J Nucl Med* 1993;34:908-917.
41. Rosenthal MS, Cullom J, Hawkins W, Moore SC, Tsui BMW, Yester M. Quantitative SPECT imaging: a review and recommendations by the Focus Committee of the Society of Nuclear Medicine Computer and Instrumentation Council. *J Nucl Med* 1995;36:1489-1513.
42. Zanzonico PB, Bigler RE, Sgouros G, Strauss A. Quantitative SPECT in radiation dosimetry. *Semin Nucl Med* 1989;19:47-61.
43. Tsui BMW, Zhao X, Frey EC, McCartney WH. Quantitative single-photon computed tomography: basics and clinical considerations. *Semin Nucl Med* 1994;24:38-65.
44. Tsui BMW, Frey EC, Zhao X, Lalush DS, Johnson RE, McCartney WH. The importance and implementation of accurate 3D compensation methods for quantitative SPECT. *Phys Med Biol* 1994;39:509-530.
45. Schold SC Jr, Zalutsky MR, Coleman RE, et al. Distribution and dosimetry of I-123 labeled monoclonal antibody 81C6 in patients with anaplastic glioma. *Invest Radiol* 1993;28:488-496.
46. Parker JA. Quantitative SPECT: basic theoretical considerations. *Semin Nucl Med* 1989;19:3-12.
47. Budinger TF. Physical attributes of single photon tomography. *J Nucl Med* 1980;21:579-592.
48. Gullberg GT, Budinger TF. The use of filtering methods to compensate for constant attenuation in single photon emission computed tomography. *IEEE Trans Biomed Eng* 1981;28:142-157.
49. Jaszczak RJ, Coleman RE, Whitehead FR. Physical factors affecting quantitative measurements using camera-based single photon emission computed tomography. *IEEE Trans Nucl Sci* 1981;28:69-80.
50. Tanaka E, Toyama H, Murayama H. Convolutional image reconstruction for quantitative single photon emission computed tomography. *Phys Med Biol* 1984;29:1489-1500.
51. Mas J, Ben-Younes R, Bidet R. Improvement of quantification in SPECT studies by scatter and attenuation compensation. *Eur J Nucl Med* 1989;15:351-356.
52. King MA, Schwinger RB, Doherty PW, Penney BC. Variation of the count-dependent Metz filter with imaging system modulation transfer function. *Med Phys* 1986;25:139-140.
53. Gilland DR, Tsui BMW, Perry JR, et al. Optimum filter function for SPECT imaging. *J Nucl Med* 1988;29:643-650.
54. Koral KF, Zasadny KR, Kessler ML, et al. A method using CT-SPECT fusion plus conjugate views for dosimetry in ^{131}I -MoAb therapy of lymphoma patients. *J Nucl Med* 1994;35:1714-1720.
55. Chang LT. A method attenuation correction in radionuclide computed tomography. *IEEE Trans Nucl Sci* 1978;NS-25:638-642.
56. Frey EC, Tsui BM, Perry JR. Simultaneous acquisition of emission and transmission data for improved Tl-201 cardiac SPECT imaging using a Tc-99m transmission source. *J Nucl Med* 1992;33:2238-2245.
57. Tan P, Bailey DL, Meikle SR, Eberl S, Fulton RR, Huton BF. A scanning line source for simultaneous emission and transmission measurements in SPECT. *J Nucl Med* 1993;34:1752-1760.
58. Manglos SH, Bassano DA, Thomas FD, Grossman ZD. Imaging of the human torso using cone-beam transmission CT implemented on a rotating gamma camera. *J Nucl Med* 1992;33:150-156.
59. Jaszczak RJ, Gilland DR, Hanson MW, Jang S, Greer KL, Coleman RE. Fast transmission CT for determining attenuation maps using collimated line source, rotatable air-copper-lead attenuators and fan-beam collimation. *J Nucl Med* 1993;34:1577-1586.
60. Tung C-H, Gullberg GL, Zeng GL, Christian PE, Datz FL, Morgan HT. Non-uniform attenuation correction using simultaneous transmission and emission converging tomography. *IEEE Trans Nucl Sci* 1992;39:1134-1143.
61. Ficaro EP, Fessler JA, Rogers WL, Schwaiger M. Comparison of Am-241 and Tc-99m as transmission source for the attenuation correction of Tl-201 SPECT imaging of the heart. *J Nucl Med* 1994;35:652-663.
62. Stewart R, Ponto R, Dickinson C, Meakem L, Chava R, Juni J. In-vivo validation of simultaneous transmission-emission protocol (STEP) for Tc-99m-sestamibi SPECT-quantitative comparison with N-13-ammonia PET [Abstract]. *J Am Coll Cardiol* 1995;25:217A.
63. Miron S, Conant R, Sodee D, Amini S. Clinical evaluation of simultaneous transmission SPECT myocardial perfusion images (STEP) [Abstract]. *J Nucl Med* 1995;36:12P.
64. Nickoloff EL, Perman WH, Esser PD, Bashist B, Alderson PO. Left ventricular volume: physical basis for attenuation corrections in radionuclide determinations. *Radiology* 1981;152:511-515.
65. Pelizzari CA, Chen GTY, Spelbring DR, Weichselbaum RR, Chen CT. Accurate three-dimensional registration of CT, PET, and/or MRI images of the brain. *J Comput Assist Tomogr* 1989;14:20-26.
66. Weber DA, Ivanovic M. Correlative image registration. *Semin Nucl Med* 1994;24:311-323.
67. Parsai EI, Ayyangar KM, Dobelbower RR, Siegel JA. Clinical fusion of three-dimensional images using bremsstrahlung SPECT and CT. *J Nucl Med* 1997;38:319-324.
68. Manglos SJ, Jaszczak RJ, Floyd CE. Weighted backprojection implemented with a nonuniform attenuation map for improved SPECT quantitation. *IEEE Trans Nucl Sci* 1988;NS-35:625-628.
69. Tsui BMW, Gullberg GT, Edgerton ER, et al. Correction of nonuniform attenuation in cardiac SPECT imaging. *J Nucl Med* 1989;30:497-507.
70. Fessler JA, Hero AO. Space-alternating generalized expectation-maximization algorithm. *IEEE Trans Sig Proc* 1994;42:2664-2677.
71. Ficaro EP, Fessler JA, Shreve PD, Kritzman JN, Rose PA, Corbett JR. Simultaneous transmission/emission myocardial perfusion tomography. Diagnostic accuracy of attenuation-corrected ^{99m}Tc -sestamibi single-photon emission computed tomography. *Circulation* 1996;93:463-473.
72. Jaszczak RJ, Greer KL, Floyd CE, et al. Improved SPECT quantification using compensation for scattered photons. *J Nucl Med* 1984;25:893-900.
73. Gilardi MC, Bettinardi V, Todd-Pokropek A, et al. Assessment and comparison of three scatter correction techniques in single photon emission computed tomography. *J Nucl Med* 1988;29:1971-1979.
74. Axelsson B, Maski P, Israelsson A. Subtraction of Compton-scattered photons in single photon emission computed tomography. *J Nucl Med* 1984;25:490-494.
75. Frey EC, Tsui BMW. A practical method for incorporating scatter in a projector-back-projector for accurate scatter compensation in SPECT. *IEEE Trans Nucl Sci* 1993;NS-40:1107-1116.
76. Smith MF, Jaszczak RJ. Generalized dual-energy-window scatter compensation in spatially varying media for SPECT. *Phys Med Biol* 1994;39:531-546.
77. Liang X. Compensation for attenuation, scatter, and detector response in SPECT reconstruction via iterative FBP methods. *Phys Med Biol* 1993;20:1097-1106.
78. Ljungberg M, Msaki P, Strand SE. Comparison of dual-window and convolution scatter correction techniques using the Monte Carlo method. *Phys Med Biol* 1990;35:1099-1110.
79. Logan KW, McFarland WD. Single photon scatter compensation by photopeak energy distribution analysis. *IEEE Trans Nucl Sci* 1991;38:1178-1182.
80. Koral KF, Swaillem FM, Buchbinder S, Clinthorne NH, Rogers WL, Tsui BMW. SPECT dual-energy window Compton correction: scatter multiplier required for quantification. *J Nucl Med* 1990;31:893-900.
81. Bayouth JE, Macey DJ. Quantitative imaging of holmium-166 with an Anger camera. *Phys Med Biol* 1994;39:265-297.
82. Koral KF, Wang X, Rogers WL, Clinthorne NH, Wang X. SPECT Compton-scattering correction by analysis of energy spectra. *J Nucl Med* 1988;29:195-202.
83. Wang X, Koral KF. A regularized deconvolution-fitting method for Compton-scatter correction in SPECT. *IEEE Trans Med Imag* 1992;11:351-360.
84. Floyd CE, Jaszczak RJ, Greer KL, et al. Deconvolution of Compton scatter in SPECT. *J Nucl Med* 1985;26:403-408.
85. Msaki P, Axelsson B, Dahl CM, Larsson SA. Generalized scatter correction method in SPECT using point scatter distribution functions. *J Nucl Med* 1987;28:1861-1869.
86. Ljungberg M, Strand S-E. Scatter and attenuation correction in SPECT using density maps and Monte Carlo simulated scatter functions. *J Nucl Med* 1990;31:1560-1567.
87. Floyd J, Mann R, Shaw A. Changes in quantitative SPECT thallium-201 results

- associated with the use of energy-weighted acquisition. *J Nucl Med* 1991;32:805-807.
88. Staff RT, Gemmell HG, Sharp PF. Assessment of energy-weighted acquisition in SPECT using ROC analysis. *J Nucl Med* 1995;36:2352-2355.
 89. O'Connor MK, Caiti C, Christian TF, Gibbons RJ. Effects of scatter correction on the measurement of infarct size from SPECT cardiac phantom studies. *J Nucl Med* 1995;36:2080-2086.
 90. Floyd CE, Jaszczak RJ, Greer KL, Coleman RE. Inverse Monte Carlo as a unified reconstruction algorithm for ECT. *J Nucl Med* 1986;27:1577-1585.
 91. Koral KF. Editorial: correction for patient Compton-scattering—current status. *J Nucl Med* 1991;32:1291-1293.
 92. Frey E, Li J, Tsui B. The importance of combined scatter and attenuation compensation in Tl-201 cardiac SPECT [Abstract]. *J Nucl Med* 1995;36:60P.
 93. King MA, Xia W, DeVries DJ, et al. A Monte Carlo investigation of artifacts caused by liver uptake in single-photon emission computed tomography perfusion imaging with technetium 99m-labeled agents. *J Nucl Cardiol* 1996;3:18-29.
 94. Iosilevsky G, Israel O, Frenkel A, et al. A practical SPECT technique for quantitation of drug delivery to human tumors and organ absorbed radiation dose. *Semin Nucl Med* 1989;19:33-46.
 95. Pretorius PH, van Aswegen AI, Herbst CP, Lotter MG. The effects of different correction techniques on absolute volume determination with SPECT using a threshold edge detection method. *Med Phys* 1991;18:390-393.
 96. Erdi YE, Wessels BW, Loew MH, Erdi AK. Threshold estimation in single photon emission computed tomography and planar imaging for clinical radioimmunotherapy. *Cancer Res* 1995;55(suppl):5823s-5826s.
 97. Pretorius PH, van Aswegen A, Lotter MG, et al. Verification of a varying threshold edge detection SPECT technique for spleen volume: a comparison with computed tomography volumes. *J Nucl Med* 1993;34:963-967.
 98. Long DT, King MA, Penney BC. 2D vs. 3D edge detection as a basis for volume quantitation in SPECT. In: Ortendahl DA, Llacer J, eds. *Information processing in medical imaging*. New York: Wiley Liss; 1991:457-471.
 99. King MA, Long DT, Brill AB. SPECT volume quantitation: influence of spatial resolution, source size and shape, and voxel size. *Med Phys* 1991;18:1016-1024.
 100. Long DT, King MA, Sheehan J. Comparative evaluation of image segmentation method for volume quantitation in SPECT. *Med Phys* 1992;19:483-490.
 101. Glick SJ, Penney BC, King MA, Byrne CL. Noniterative compensation for the distance dependent detector response and photon attenuation in SPECT imaging. *IEEE Trans Med Imag* 1994;13:363-374.
 102. Gilland DR, Jaszczak RJ, Turkington TG, Greer KL, Coleman RE. Volume and activity quantitation with iodine-123 SPECT. *J Nucl Med* 1994;35:1707-1713.
 103. Mortelmans L, Nuyts J, Van Pamel G, Van den Maegdenbergh V, De Roo M, Suetens P. A new thresholding method for volume determination by SPECT. *Eur J Nucl Med* 1986;12:284-290.
 104. Sgouros G, Chiu S, Pentlow KS, et al. Three-dimensional dosimetry for radioimmunotherapy treatment planning. *J Nucl Med* 1993;34:1595-1601.
 105. Sgouros G, Barest G, Thekkumthala J, et al. Treatment planning for internal radionuclide therapy: three-dimensional dosimetry for nonuniformly distributed radionuclides. *J Nucl Med* 1990;31:1884-1891.
 106. Giap HB, Macey DJ, Podoloff DA. Development of a SPECT-based three-dimensional treatment planning system for radioimmunotherapy. *J Nucl Med* 1995;36:1885-1894.
 107. Furhang EE, Chui C, Sgouros G. A Monte Carlo approach to patient-specific dosimetry. *Med Phys* 1996;23:1523-1529.
 108. Kolbert KS, Sgouros G, Scott AM, et al. Implementation and evaluation of patient-specific three-dimensional internal dosimetry. *J Nucl Med* 1997;38:301-308.
 109. Hoffman EJ, Phelps ME. Positron emission tomography: principles and quantitation. In: Phelps ME, Mazziotta J, Schelbert H, eds. *Positron emission tomography and autoradiography: principles and applications for the brain and heart*. New York: Raven Press; 1986:237-286.
 110. Larson SM, Pentlow KS, Volkow ND, et al. PET scanning of iodine-124-3F9 as an approach to tumor dosimetry during treatment planning for radioimmunotherapy in a child with neuroblastoma. *J Nucl Med* 1992;33:2020-2023.
 111. Leichner PT, Klein JL, Garrison LB, et al. Dosimetry of ¹³¹I-labeled anti-ferritin in hepatoma: a model for radioimmunoglobulin dosimetry. *Int J Radiat Oncol Phys* 1981;7:323-333.
 112. Cohn SH. Whole body counters. In: Editors: Wagner HN, Szabo Z, Buchanan JW. *Principles of nuclear medicine*, 2nd ed. Philadelphia: W.B. Saunders; 1995:298-305.
 113. Lathrop KA, Harper PV, Charleston DB, Atkins FB, Mock BH. Acquisition of quantitative biologic data in humans for radiation absorbed dose estimates. In: Cloutier RJ, Coffey JL, Snyder WS, Watson EE, eds. *Radiopharmaceutical dosimetry symposium. Proceedings of a conference held at Oak Ridge, TN, April 26-29, 1976*. Washington: U.S. Government Printing Office 1976:164-173.
 114. Sgouros G. Bone marrow dosimetry for radioimmunotherapy: theoretical considerations. *J Nucl Med* 1993;34:689-694.
 115. Lee RE, Siegel JA, Horowitz JA, et al. The use of SPECT in monoclonal antibody imaging to determine marrow-to-blood activity concentration ratio [Abstract]. *J Nucl Med Technol* 1990;18:143.
 116. Fisher DR. Radiation dosimetry for radioimmunotherapy. *Cancer Suppl* 1994;73:905-911.
 117. Cloutier RJ, Smith EA, Watson EE, et al. Dose to the fetus from radionuclides in the bladder. *Health Phys* 1973;25:147-161.
 118. Thomas SR, Stabin MG, Chen C, Samaritunga RC. MIRD Pamphlet No. 14 Revised: a dynamic urinary bladder model for radiation dose calculations. *J Nucl Med* 1999;40:Forthcoming April.
 119. *Limits for intakes of radionuclides by workers*. Annals of the ICRP, 2, ICRP Publication 30 (Part 1). Oxford: Pergamon Press; 1979:30-34.
 120. Stubbs JB. Results from a new mathematical model of gastrointestinal transit that incorporates age and gender-dependent physiological parameters. *Radiat Protein Dosim* 1992;41:63-69.
 121. Stubbs JB, Marshall BJ. Radiation dose estimates for the carbon-14-labeled urea breath test. *J Nucl Med* 1993;34:821-825.
 122. Bers L. *Calculus*. New York: Holt, Rinehart, and Winston, Inc; 1969:413-416.
 123. Macon N. *Numerical analysis*. New York: Wiley; 1963.
 124. Riggs DS. *The mathematical approach to physiological problems*. Cambridge, MA: The M.I.T. Press; 1976.
 125. Jacquez JA. *Compartmental analysis in biology and medicine*. Ann Arbor: The University of Michigan Press; 1985.
 126. Feldman HA. A numerical method for fitting compartmental models directly to tracer data. *Am J Physiol* 1977;233:R1-R7.
 127. D'Argenio DZ, Schumitzky A. A program package for simulation and parameter estimation in pharmacokinetic systems. *Comput Prog Biomed* 1979;9:115-134.
 128. Karayanakis NM. *Advanced system modelling and simulation with block diagram languages*. Boca Raton, FL: CRC Press; 1995.
 129. Hays MT. Radiation dosimetry of radioiodinated thyroid hormones. *J Nucl Med* 1985;25:1068-1074.